

PRODUCTION OF  $K_L^0$  MESONS AND NEUTRONS FROM  
ELECTRONS ON BERYLLIUM ABOVE 10 GeV\*

G. W. Brandenburg, A. D. Brody, W. B. Johnson, D.W.G.S. Leith  
J. S. Loos\*\*, G. J. Luste\*\*\*, J.A.J. Matthews, K. Moriyasu†  
B. C. Shen††, W. M. Smart†††, F. C. Winkelmann, and R. J. Yamartino  
Stanford Linear Accelerator Center  
Stanford, University, Stanford, California 94305

ABSTRACT

Measurements are presented of the yields of  $K_L^0$  mesons and neutrons produced by electrons of energies between 10 and 19 GeV incident on 0.70 and 1.75 radiation length beryllium targets for production angles between  $1.6^\circ$  and  $4^\circ$ . Values for the  $K_L^0$  absorption cross section on lead are also found for momenta between 1.4 and 7.4 GeV/c. A successful interpretation of  $K_L^0$  production is made in terms of the process  $\gamma N \rightarrow K_L^0 X$ , where X represents an inclusive sum over all final states. The invariant structure function for  $K_L^0$  photoproduction, extracted from the Be yields, is found to be simply related to the result for hydrogen by an overall multiplicative factor,  $A_{EFF}$ , the effective number of nucleons in the target nucleus. The results of the theoretical analysis are also compared to charged K photoproduction and extrapolated to electron energies of 50 GeV.

(Submitted to Phys. Rev.)

---

\* Work supported in part by the U.S. Atomic Energy Commission.  
\*\* Now at Duke University, Durham, North Carolina.  
\*\*\* Now at the University of Toronto, Toronto, Canada.  
† Now at the University of Washington, Seattle, Washington.  
†† Now at the University of California (Riverside), Riverside, California.  
††† Now at the National Accelerator Laboratory, Batavia, Illinois.

## I. Introduction

We present measurements of the yield of  $K_L^0$  mesons and neutrons produced from electrons incident on a beryllium target at energies between 10 and 19 GeV. Table 1 summarizes the specific electron energies, production angles, and Be target thicknesses for which these measurements have been made. The data were acquired during three separate data runs at the Stanford Linear Accelerator Center (SLAC) in which the SLAC 40-inch hydrogen filled bubble chamber was exposed to a neutral beam. A description of the neutral beam is given in Section II. A preliminary report of the results for run I is given in Ref. 1. Measurements of  $K_L^0$  photoproduction below 10 GeV on complex nuclei have also been made in other experiments.<sup>2-5</sup>

The yields of  $K_L^0$  and neutrons are presented in Sections III and IV respectively. The yields are found to behave similarly above  $\sim 4$  GeV/c, where both show a rapid fall off with increasing momentum of the neutral particle. However, for momenta below  $\sim 2$  GeV/c the neutron yield has an intense low energy component which is not present in the  $K_L^0$  yield. This low energy component is probably due to the disintegration of the target nucleus.

The present measurements of  $K_L^0$  yields together with previous measurements<sup>1-3</sup> suggest that the photoproduction of  $K^0$  mesons is a complicated process with contributions not only from the obvious two-body and quasi-two-body reactions but also from multiparticle channels. A natural framework for dealing with such a complicated situation is provided by the inclusive single particle production process,  $\gamma N \rightarrow K_L^0 X$ , where X represents the sum of all final state configurations. In Section V, we discuss the  $K_L^0$  yields in terms of inclusive  $K_L^0$  production and find a satisfactory description for the measurements. Extrapolations are then

made for  $K_L^0$  yields at higher energies and for various target thicknesses. Comparisons are also made to the available yield data for  $K^+$  and  $K^-$  mesons.

## II. Neutral Secondary Beam

A schematic illustration of the neutral beam is shown in Fig. 1. The primary electron beam first passed through a toroid charge monitor<sup>(6)</sup> which integrated the total charge per pulse for purposes of beam normalization. The production angle of the neutral beam with respect to the electron beam could be varied from  $1.5^\circ$  to  $5^\circ$  by a dipole magnet placed immediately upstream of the Be target. The position, spot size, and angle of entry of the electron beam on the target was monitored visually by means of closed-circuit television displays of two ruled zinc sulfide screens. The first screen was attached to the upstream face of the target and the second was attached to the upstream face of a water cooled dump used to stop the electron beam. The neutral beam channel was defined by three carefully aligned lead collimators: a 2.2 meter tapered collimator centered 7 meters from the target, and two 0.5 meter untapered collimators located 10 meters and 22 meters from the target. Two sweeping magnets were used to remove charged particles. The halo of muons was absorbed by  $\sim 15$  meters of iron shielding surrounding the neutral beam channel. The photons in the beam were absorbed by placing suitable amounts of material in the beam, as summarized in Table 2. At the bubble chamber (55 meters from the target) the beam had a cross sectional area of 15 cm by 40 cm and subtended a solid angle of  $\sim 2 \times 10^{-5}$  sr.

## III. $K_L^0$ Yields

### A. Selection of Events

The film was scanned for the visible  $K_L^0$  decays:  $K_L^0 \rightarrow \pi^\pm e^\mp \nu$ ,  $K_L^0 \rightarrow \pi^\pm \mu^\mp \nu$ , and  $K_L^0 \rightarrow \pi^+ \pi^- \pi^0$ . These decays appear mainly as two-prong events which are not associated with any interaction in the chamber. However, a small fraction of the final sample of events (8%) were first classified by the scanners as associated

with an interaction in the chamber but were properly reclassified as beam decays following measurement. The decay tracks were measured either on the SLAC spiral reader or on film plane digitizers, and spatially reconstructed with the program TVGP. The reconstructed tracks and the  $K_L^0$  direction were then used to obtain kinematic solutions to the above decay modes. Events were included in the analysis of the  $K_L^0$  momentum spectrum if any of the 5 decay modes was kinematically possible.<sup>(7)</sup> Events were excluded if any of the following were satisfied:

$$M(e^+e^-) < 35 \text{ MeV},$$

$$485 < M(\pi^+\pi^-) < 510 \text{ MeV},$$

or 
$$1110 < M(p\pi^-) < 1120 \text{ MeV},$$

where the charged tracks were interpreted as the indicated particles. These cuts, which effectively remove all non- $K_L^0$  decays, also remove a small fraction ( $\sim 5\%$ ) of the  $K_L^0$  decays. However, these cuts introduce no bias since the same cuts are made on the Monte Carlo events used in the theoretical analysis (see below). A final selection required the  $K_L^0$  decay to occur within a 55 cm long decay volume within the chamber.

#### B. Determination of the $K_L^0$ Momentum Spectrum at the Bubble Chamber.

The method of analysis described below determines both the shape and the absolute magnitude of the  $K_L^0$  momentum spectrum at the bubble chamber from the observed distribution of the visible momentum,  $p_{\text{VIS}}$ , defined as

$$p_{\text{VIS}} = \hat{n} \cdot (\vec{p}_1 + \vec{p}_2),$$

where  $\vec{p}_1$  and  $\vec{p}_2$  are the three-momenta of the two charged tracks and  $\hat{n}$  is a unit vector along the beam direction. On the average, the quantity  $p_{\text{VIS}}$  is roughly two thirds of the  $K_L^0$  momentum,  $p_K$ , regardless of decay mode; therefore, the  $p_{\text{VIS}}$  distribution depends sensitively on the shape of the  $p_K$  distribution. The absolute

intensity of the  $K_L^0$  flux is fixed by the known  $K_L^0$  lifetime and the branching ratio  $(K_L^0 \rightarrow \text{charged})/(K_L^0 \rightarrow \text{all})$ .<sup>(8)</sup>

In Fig. 2, we illustrate the procedure used to determine the momentum distribution of the  $K_L^0$  particles which decay in the chamber. First the  $p_{\text{VIS}}$  data are binned such that for the  $i^{\text{th}}$  bin there are  $N_i$  events between  $p_{\text{VIS}_i}$  and  $p_{\text{VIS}_i} + \Delta p_{\text{VIS}_i}$ . The momentum distribution of decays, denoted  $Z(p_K)$ , is then represented by a histogram, the  $j^{\text{th}}$  bin of which covers the interval from  $p_{K_j}$  to  $p_{K_j} + \Delta p_{K_j}$ . The height of the  $j^{\text{th}}$  bin,  $Z(p_{K_j})$ , is denoted by the parameter  $\alpha_j$ . For each bin in  $p_K$ , a  $p_{\text{VIS}}$  distribution is then generated by Monte Carlo techniques,<sup>(9)</sup> for the  $j^{\text{th}}$  bin in  $p_K$  the  $p_{\text{VIS}}$  distribution normalized to unity is denoted  $H_{ji}$ , where the index  $i$  runs over all  $p_{\text{VIS}}$  bins. Each  $p_{\text{VIS}}$  distribution is comprised of events from the five main  $K_L^0$  charged decay modes generated according to the standard decay matrix elements in proportion to their known decay rates.<sup>(8)</sup> The mass cuts used for the data selection (see Sect. III-A) are also applied to the Monte Carlo events. For an assumed set of  $\alpha_j$  values, the expected number of events in the  $i^{\text{th}}$   $p_{\text{VIS}}$  bin is then given by:

$$T_i = \sum_j \alpha_j H_{ji}.$$

The best set of values for the  $\alpha_j$ 's is then determined by minimizing  $\chi^2(\alpha_1, \alpha_2, \dots)$ , where

$$\chi^2(\alpha_1, \alpha_2, \dots) \equiv \sum_i (T_i - N_i)^2 / T_i.$$

The value of  $\alpha_j$  at the minimum of  $\chi^2$ ,  $\alpha_j^*$ , is equal to  $Z(p_{K_j})$ .<sup>(10)</sup> In order to determine the statistical uncertainties in  $\alpha_j^*$ , a number of successive reminimizations of  $\chi^2$  (typically 50) are done after independently changing each  $p_{\text{VIS}}$  bin from its original value,  $T_i$ , to  $T_i \pm \delta T_i$  where  $\delta T_i$  is randomly chosen on successive minimizations according to a gaussian distribution having a standard deviation equal to  $T_i^{1/2}$ . The standard deviations of the values of  $\alpha_j^*$  thus obtained are taken to be

the statistical uncertainties.

The procedure outlined above is illustrated in Fig. 2 for a  $K_L^0$  beam produced at  $2^\circ$  by 16 GeV electrons on a 1.75 radiation length (r.l.) Be target. The  $p_{VIS}$  distributions corresponding to the fitted components of the  $Z(p_K)$  distribution are summed to provide the solid curve on the experimental  $p_{VIS}$  distribution. This curve is seen to reproduce the  $p_{VIS}$  spectrum very well.

The absolute flux of  $K_L^0$  at the chamber, denoted by  $F(p_K)$ , is related to  $Z(p_K)$  as follows:

$$F(p_K) = \frac{1}{\epsilon r} \left[ 1 - e^{-L/\lambda(p_K)} \right]^{-1} Z(p_K)$$

where

- $\epsilon$  = efficiency factor for scanning and measuring of the film,
- $r$  = branching ratio,  $(K_L^0 \rightarrow \text{charged}) / (K_L^0 \rightarrow \text{all})$ ,
- $\lambda(p_K) = \frac{p_K c \tau}{m_K}$ , the mean  $K_L^0$  decay length,
- $L$  = length of decay volume in the chamber,
- $m_K$  =  $K_L^0$  mass,

and

- $\tau$  =  $K_L^0$  lifetime.

An example of the  $K_L^0$  flux at the chamber is shown in Fig. 3. The uncertainties shown are the statistical uncertainties determined as described above.

As a check of the preceding method we have also determined the  $K_L^0$  spectrum at the chamber by an alternate method.<sup>(11)</sup> First, by means of a transverse momentum selection, a sample of unique  $K_{e3}$  decays is isolated. This selection retains approximately 15% of the total number of  $K_L^0$  decays. Each of these decays has up to four kinematical solutions for  $p_K$ , and each of the solutions is assigned a weight which is normalized such that the total weight for a single decay is unity. The individual weights are proportional to a product of the Dalitz plot density, the Jacobian relating  $p_K$  to the measured variables, and the  $K_L^0$  spectrum. Thus the

spectrum is given by:

$$Z(p_{Kj}) = \sum_{i=1}^{N_j} W_{ij}(Z),$$

where the  $W_{ij}(Z)$  are the weights of the  $N_j$  kinematical solutions in the  $j^{\text{th}}$   $p_K$  bin. Since the weights are functions of the  $K_L^0$  spectrum ( $Z$ ), this expression is a set of  $m$  non-linear equations, where  $m$  is the number of  $p_K$  bins. These can be solved iteratively by substituting the spectrum  $Z$  of the previous iteration into  $W_{ij}(Z)$  to obtain a new solution. Using an arbitrary spectrum as a starting value, this procedure converges after a few iterations to a unique solution for  $Z(p_K)$ . The open circles in Fig. 3 show a  $K_L^0$  spectrum obtained by this method, where  $Z(p_K)$  has been converted to flux at the chamber. The agreement with the previously described spectrum determination is excellent, although the error bars are larger due to the smaller statistics.

### C. Determination of $K_L^0$ Yields at the Target from $K_L^0$ Fluxes at the Chamber

If  $F(p_K)$  is the flux of  $K_L^0$  mesons per GeV/c at the chamber,  $D$  the distance between target at chamber,  $\Delta\Omega$  the solid angle of the detector, and  $N_e$  the number of electrons incident on the target, then the yield is given by

$$Y_K(p_K) = F(p_K) \exp [D/\lambda(p_K)] \exp \left[ \sum_i a_i \sigma_{Ki}(p_K) \right] / (N_e \Delta\Omega),$$

expressed in units of  $K_L^0$ /electron/sr/GeV/c. The first exponential factor corrects for the loss of  $K_L^0$  particles due to decays in flight. The second exponential factor corrects for absorption of the  $K_L^0$  beam in the photon absorbers (see Table 2), where for the  $i^{\text{th}}$  absorber,  $\sigma_{Ki}(p_K)$  is the total  $K_L^0$  absorption cross section for momentum  $p_K$ ,  $a_i = \rho_i N_o / A_i$ ,  $\rho_i$  is the amount of absorber in  $\text{g/cm}^2$ ,  $A_i$  is the atomic weight, and  $N_o$  is Avogadro's number.

The solid angle factor,  $\Delta\Omega$ , has been determined from the geometry of the neutral beam; corrections for collimator edges have been made by a study of the

distribution of  $K_L^0$  decay positions within the bubble chamber. The number of incident electrons,  $N_e$ , has been measured for each accelerator pulse in the toroid charge monitor and summed over the pulses for each yield curve.

Values for the absorption cross sections for Li, W, and Pb have been interpolated from the  $K_L^0$ -nucleus measurements of Lakin et al.,<sup>(12)</sup> and the  $K^\pm$ -nucleus measurements of Abrams et al.<sup>(13)</sup> In addition, values for the  $K_L^0$ -Pb absorption cross section have been measured in the present experiment and are presented in Table 3.<sup>(14)</sup> The available K-nucleus cross sections are shown in Fig. 4 together with interpolation curves which, for atomic weight A and momentum  $p_K$ , are given by the empirical parameterization<sup>(15)</sup>

$$\sigma(p_K, A) = [b_1(p_K + b_2A)^{-n_1} + b_3] A^{n_2}. \quad (1)$$

Values for the  $K_L^0 p$  absorption cross section have been interpolated from  $K^\pm n$  measurements,<sup>(16-18)</sup> also shown in Fig. 4, where the interpolation curve is of the form<sup>(15)</sup>

$$\sigma(p_K) = b_4 p_K^{-n_3} + b_5.$$

The  $K_L^0$  yield results for the 1.75 r.l. Be target are presented in Table 4 and Fig. 5; the results for the 0.70 r.l. Be target are presented in Table 5 and Fig. 6. The quoted uncertainties are the statistical uncertainties in  $F(p_K)$ , discussed in Sect. III-B. All the yield curves have a broad maximum for  $p_K$  equal to  $\sim 15\%$  of the incident electron energy. The fall off in yield at larger  $p_K$  values becomes more rapid as the target thickness is increased and as the production angle is increased. The curves shown on Figs. 5 and 6 are discussed in detail in Section V. D. Estimates of Systematic Uncertainties in the  $K_L^0$  Yields.

The relative systematic uncertainties between the various  $K_L^0$  yields are estimated to be 15%, with the following contributions taken in quadrature: film



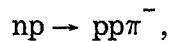
analysis (5%), solid angle (5%), and targetting (focus and intensity) of the electron beam (10%).

The overall systematic uncertainty in the scale of the  $K_L^0$  yields is estimated to be 20%, and is comprised of  $\sim 15\%$  uncertainty in the absorption factor and  $\sim 10\%$  uncertainty in the film analysis.

#### IV. Neutron Yields

##### A. Selection of Events

The neutron flux at the bubble chamber has been determined from a sample of events from the reaction



which appear as three-prong interactions in the chamber. The candidates have been measured on the SLAC spiral reader, and spatially reconstructed and kinematically fitted with the programs TVGP and SQUAW. These events have three kinematic constraints since the direction of the beam and the momenta of all outgoing tracks are measured. For momenta above  $\sim 5$  GeV/c, a fraction of the events ( $\sim 10 - 15\%$ ) are kinematically ambiguous with the reaction  $K^0 p \rightarrow pK^+ \pi^-$ . However, the majority of the ambiguities are resolved on the basis of the  $\chi^2$  probabilities of the kinematic fits, and we estimate that the remaining contamination from the  $K^0 p$  events is less than 5% at all momenta. The same samples of film and the same active volume in the chamber were used for the  $np \rightarrow pp\pi^-$  events as for the  $K_L^0$  decays.

##### B. Determination of the Neutron Momentum Spectrum at the Bubble Chamber.

For a given neutron momentum,  $p_n$ , the neutron flux at the chamber per GeV/c is given by:

$$F(p_n) = C N(p_n) / \sigma(np \rightarrow pp\pi^-)$$

where  $N(p_n)$  is the number of observed  $np \rightarrow pp\pi^-$  events per GeV/c, and the

constant of proportionality,  $C$ , is determined from the density of the liquid hydrogen and the length of the interaction region.

Values for  $\sigma(np \rightarrow pp\pi^-)$  have been interpolated from the pd experiments of Batson et al<sup>(19)</sup>, Cohn et al,<sup>(20)</sup> Brunt et al,<sup>(21)</sup> Shapira et al,<sup>(22)</sup> and Rushbrooke et al<sup>(23)</sup> and from the np experiment of Gasparyan et al.<sup>(24)</sup> These cross section data are plotted in Fig. 7 together with a hand drawn interpolation curve (solid curve) used for the present analysis. The dashed curves represent our estimate of the uncertainty of the interpolation curve.

An example of the neutron flux at the chamber is shown in Fig. 3 for comparison to the  $K_L^0$  flux. The uncertainties shown are dominated by the uncertainty in  $\sigma(np \rightarrow pp\pi^-)$  rather than the statistical error on  $N(p_n)$ . The neutron flux peaks below 1 GeV/c and the  $n/K_L^0$  ratio is seen to decrease by an order of magnitude over the range from 2 to 6 GeV/c. For this example the flux of neutrons becomes equal to the flux of  $K_L^0$  mesons for  $p \sim 3$  GeV/c. However, the  $n/K_L^0$  ratio at the chamber depends on the amount of absorber in the neutral beam and is diminished as the amount of absorber is increased since the nuclear absorption cross sections are larger for neutrons than for  $K_L^0$  mesons.

#### D. Determinations of Neutron Yields at the Target from Neutron Fluxes at the Chamber

If  $F(p_n)$  is the number of neutrons per GeV/c at the chamber,  $\Delta\Omega$  the solid angle of the detector, and  $N_e$  the number of electrons incident on the target, then the yield is given by

$$Y_n(p_n) = F(p_n) e^{\sum_i a_i \sigma_{ni}(p_n)} / (N_e \Delta\Omega),$$

expressed in units of neutrons/electron/sr/GeV/c. The same values for  $N_e$ ,  $\Delta\Omega$ , and the  $a_i$ 's apply to the neutron yields as applied to the  $K_L^0$  yields (see Sect. III. C).

Values for neutron absorption cross sections for Li, W, and Pb have been interpolated from the measurements of Refs. 12, 25 - 30. Values for np total cross

sections have been interpolated from the measurements of Refs. 31 - 33.

The results for the neutron yields are given in Table 6 and Fig. 8. The quoted uncertainties are the sum in quadrature of the statistical uncertainty in  $N(p_n)$  and the estimated uncertainty of the interpolation curve for  $\sigma(p_n)$  shown in Fig. 7. The neutron yields have an intense low energy component below  $\sim 2$  GeV/c. Since this low energy component is not present in the  $K_L^0$  yields, it must arise from the disintegration of Be nuclei in the target. For momenta above  $\sim 4$  GeV/c the yield of neutrons and  $K_L^0$  mesons from the 1.75 r.l. Be target have similar dependences on momentum, with the ratio  $n/K_L^0$  being in the range  $\sim 1.2$  to  $\sim 1.7$ .

#### D. Estimates of Systematic Uncertainties in the Neutron Yields.

The relative systematic uncertainties between the various neutron yields is estimated to be 15%, the same as for the relative systematic uncertainty between the various  $K_L^0$  yields (see Sect. III-D).

The overall systematic uncertainty in the scale of the neutron yields is estimated to be 20%, and is made up of  $\sim 15\%$  uncertainty in the absorption factor, and  $\sim 10\%$  uncertainty in the film analysis.

### V. Interpretation of $K_L^0$ Yields

#### A. Theoretical Analysis

The production of hadronic particles from high energy electrons incident on thick targets can be described qualitatively by the following sequence of steps: (a) real photons<sup>(34)</sup> are produced by bremsstrahlung throughout the volume of the target, (b) particles are photoproduced from the target nuclei, and (c) a fraction of the hadronic particles are absorbed before leaving the target. Although steps (a) and (c) are well understood and readily parameterized, step (b) is in general a complicated summation over many processes, and has not been systematically parameterized in previous studies.

The aim of this section is to obtain a simple description of the measured  $K_L^0$  yields by considering only two production processes. The more important contribution is incoherent photoproduction from the individual nucleons in the target nucleus,  $\gamma N \rightarrow K_L^0 X$ , where X represents the inclusive sum over all final state configurations. The second contribution is from the reaction  $\gamma \text{Be} \rightarrow \phi(1020) \text{Be}$ ,  $\phi(1020) \rightarrow K_L^0 K_S^0$ , which we assume to be the only important coherent process for  $K_L^0$  photoproduction.

The quantitative description for steps (a)-(c) for the yield of hadronic particles having laboratory momentum,  $p$  (GeV/c), and laboratory production angle,  $\Theta$ , from a target of thickness,  $T$  (in units of r.l.), for electrons incident with energy,  $E_0$  (GeV), is given by the following relation:<sup>(35)</sup>

$$Y(p, \Theta; T, E_0) = \left( \frac{N_0 X_0}{2\pi A} \right) \int_0^T dt \int_{k_{\min}}^{E_0} dk e^{-\eta(p)(T-t)} I_\gamma(k, E_0, t) \frac{d^2\sigma(k)}{dp d\cos\Theta} \quad (2)$$

in units of particles/electron/sr/GeV/c. In this expression,  $k$  is the photon energy,  $I_\gamma(k, E_0, t)$  is the distribution in energy of the photons for a single electron of energy  $E_0$  incident on a target of thickness  $t$ ,  $\frac{d^2\sigma}{dp d\cos\Theta}$  is the differential cross section for photoproduction of the hadronic particles,  $k_{\min}$  is the minimum energy kinematically allowed,  $N_0$  is Avagadro's number,  $X_0$  is the unit r.l. of the target material in  $\text{gr/cm}^2$ , and  $A$  is the atomic weight of the target nucleus. The factor  $\eta(p)$  accounts for the absorption of the hadronic particles leaving the target and is given by

$$\eta(p) = \left( \frac{N_0 X_0}{A} \right) \sigma(p),$$

where  $\sigma(p)$  is the absorption cross section for the target nucleus. For the beryllium nucleus we have used the empirical parameterization of Eq. (1) for  $\sigma(p)$ . The photon energy distribution is given by the thick-target approximation of

Tsai and Whitis:<sup>(35)</sup>

$$I_{\gamma}(k, E_0, t) = \frac{1}{k} \frac{(1 - k/E_0)^{(4/3)t} e^{-(7/9)t}}{[(7/9) + (4/3)\ln(1 - k/E_0)]} .$$

In order to describe  $K_L^0$  yields by electrons on thick targets, the single particle differential cross section for  $K_L^0$  photoproduction must be known. In the present analysis, we assume

$$\frac{d^2\sigma}{dpd\cos\Theta} = \left(\frac{d^2\sigma}{dpd\cos\Theta}\right)_{\text{incoherent}} + \left(\frac{d^2\sigma}{dpd\cos\Theta}\right)_{\text{coherent}}$$

where the incoherent part is inclusive  $K_L^0$  photoproduction from the individual nucleons and the coherent part is  $\phi(1020)$  photoproduction from the entire target nucleus.

For each measured  $K_L^0$  yield point, the value for  $\left(\frac{d^2\sigma}{dpd\cos\Theta}\right)_{\text{coherent}}$  is calculated by a Monte Carlo integration for the two-step process:  $\gamma\text{Be} \rightarrow \phi(1020)\text{Be}$ ,  $\phi(1020) \rightarrow K_L^0 K_S^0$ . The differential cross section is interpolated from the measurements of McClellan et al<sup>(36)</sup> of  $\phi(1020)$  photoproduction from complex nuclei and is assumed to be independent of energy:

$$\frac{d\sigma}{dt} (\gamma\text{Be} \rightarrow \phi(1020)\text{Be}) = 125 e^{40t} \mu\text{b}/\text{GeV}^2,$$

where  $t$  is the square of invariant momentum transfer to the Be nucleus. The branching ratio,  $(\phi(1020) \rightarrow K_L^0 K_S^0)/(\phi(1020) \rightarrow \text{all})$ , is taken to be 31%.<sup>(8)</sup> The decay angular distribution of the  $\phi(1020)$  is required to be proportional to  $\sin^2\beta$ , where  $\beta$  is the angle between the direction of the  $K_L^0$  in the  $\phi(1020)$  rest system and the direction of the  $\phi(1020)$  in the center of mass system.

The incoherent differential cross section is treated as an unknown to be determined in the present analysis. In terms of  $p_{\perp}^2$  and the variable<sup>(37)</sup>  $x = p_{\parallel}^*/p_{\text{max}}^*$ , where  $p_{\perp}$  and  $p_{\parallel}^*$  are the transverse and longitudinal momenta of the  $K_L^0$  in the center of mass system and  $p_{\text{max}}^*$  is the kinematic maximum of the center of mass

$K_L^0$  momentum, the differential cross section is:

$$\left( \frac{d^2\sigma(k)}{dp d\cos\Theta} \right)_{\text{incoherent}} = \frac{2p^2 E^*}{E p^* \max} \frac{d^2\sigma(k)}{dx dp_{\perp}^2},$$

where  $E(E^*)$  is the energy of the  $K_L^0$  in the laboratory (center of mass) system. In the notation of the invariant structure function, (37, 38) we then have

$$\frac{E^*}{\pi p^* \max} \frac{d^2\sigma(k)}{dx dp_{\perp}^2} = f(x, p_{\perp}^2, s),$$

where  $s$  is the square of the total energy in the center of mass. The integrated structure function,  $\mathcal{F}(x, s)$ , is defined by

$$\mathcal{F}(x, s) \equiv \int_0^{\infty} dp_{\perp}^2 f(x, p_{\perp}^2, s).$$

If we assume that the hypotheses of scaling (37) and factorization (39, 40) hold for all  $s$  and  $x$ , and if we parameterize the  $p_{\perp}^2$  dependence as a single exponential, we then have

$$f(x, p_{\perp}^2, s) = \mathcal{F}(x) B e^{-B p_{\perp}^2},$$

a form which is approximately obeyed by the available data on  $\pi^{\pm}$  and  $K^{\pm}$  inclusive photoproduction from hydrogen. (41, 42) For the exponential parameter we have used  $B = 4.5 \text{ GeV}^{-2}$ , a value consistent with the measurements of Boyarski et al. (42)

With these approximations, the incoherent differential cross section becomes:

$$\left( \frac{d^2\sigma}{dp d\cos\Theta} \right)_{\text{incoherent}} = \left( \frac{2\pi p^2}{E} \right) B e^{-B p_{\perp}^2} \mathcal{F}(x).$$

The object of the analysis is then to find the magnitude and shape of  $\mathcal{F}(x)$  which best reproduces the  $K_L^0$  yield data. The procedure is possible since different values of the variable  $x$  contribute to distinctly different  $K_L^0$  momenta, as is illustrated in Fig. 9. In this Figure, we show calculated  $K_L^0$  yields as a function of  $p$  (for  $\Theta = 2^\circ$ ,  $E_0 = 16 \text{ GeV}$ , and  $T = 1.75 \text{ r.l.}$ ) corresponding to successive bins in  $\mathcal{F}(x)$ , where

for  $i^{\text{th}}$  curve

$$\begin{aligned} \mathcal{F}(x) &= 1\mu b \text{ for } x_i < x < x_{i+1} \\ &= 0 \quad \text{for all other } x, \end{aligned} \quad (3)$$

and where  $x_i = (i - 1)/10$ . Note that the observed yields receive contributions from  $\mathcal{F}(x)$  only in the interval  $0 \lesssim x \lesssim 1$ .

The shape and magnitude of  $\mathcal{F}(x)$  has been determined by a  $\chi^2$  minimization procedure as follows. First, the function  $\mathcal{F}(x)$  is represented by a histogram for which the  $i^{\text{th}}$  bin covers the region  $x_i$  to  $x_{i+1}$  and has a height given by the parameter,  $\alpha_i(\mu b)$ . The incoherent yield for the  $j^{\text{th}}$  data point (corresponding to  $p = p_j$ ,  $\Theta = \Theta_j$ ,  $E_0 = E_{0j}$ , and  $T = T_j$ ) is then given by:

$$Y_{\text{incoherent}}(j) = \sum_i \alpha_i y_{ij}$$

where the  $y_{ij}$  values are found by integrating Eq. (2) using  $\mathcal{F}(x)$  as in Eq. (3). Denoting the  $j^{\text{th}}$  data point by  $D_j$ ,  $\chi^2$  for the  $j^{\text{th}}$  point is

$$\chi_j^2 = \left( \frac{D_j - S_j}{\Delta_j} \right)^2,$$

where  $S_j = Y_{\text{coherent}}(j) + Y_{\text{incoherent}}(j)$ .

The denominator,  $\Delta_j$ , is taken to be

$$\Delta_j = [ (\delta D_j)^2 + (\epsilon D_j)^2 ]^{\frac{1}{2}}$$

where  $\delta D_j$  is the statistical uncertainty quoted in Tables 4-5 and  $\epsilon = 0.10$  is our estimate of the systematic uncertainties expected between the various yield curves.

## B. Discussion of Results

The results of the best fit are displayed in Figs. 5-6. The solid curves represent the sum of the coherent and incoherent yields whereas the dashed curves represent the incoherent yields alone. The yield measurements for all energies,

production angles, and target thicknesses are observed to be satisfactorily reproduced. As seen in Figs. 5-6, the major portion of yield arises from the incoherent contributions. The coherent  $\phi(1020)$  contribution, which is  $\sim 15\%$  of the total yield at  $2^\circ$ , is concentrated at low momenta and diminishes rapidly as the production angle is increased.

The fitted values for the integrated structure function,  $\mathcal{F}(x)$ , are given in Table 7 and shown in Fig. 10. For the integral over  $x$ , we find  $\int_0^1 dx \mathcal{F}(x) = 6.0 \mu\text{b}$ . The overall systematic uncertainty in  $\mathcal{F}(x)$  may be as large as 25% arising from the overall systematic uncertainties in the data, in the thick target approximation for the photon energy spectrum, and in the theoretical assumptions of scaling and factorization.

It is interesting to compare the values of  $\mathcal{F}(x)$  for Be to those for hydrogen. In Fig. 10 we also show the preliminary data of Boyarski *et al*.<sup>(42)</sup> for the average of  $K^+$  and  $K^-$  inclusive photoproduction from hydrogen at 18 GeV.<sup>(43)</sup> The charged K results agree well in shape with the  $K_L^0$  results, differing only by a scale factor,  $A_{\text{EFF}}$ .  $A_{\text{EFF}}$  can be interpreted as the effective number of nucleons contributing to the incoherent particle production. For the present comparison we find  $A_{\text{EFF}} = 6$ , in agreement with the empirical relation,  $A_{\text{EFF}} = A^{0.9}$ , which applies over a wide range of photon energies in the measurement of  $\gamma A$  total cross sections.<sup>(44-45)</sup> Thus the inclusive photoproduction of particles from light nuclei and from hydrogen appear to be related simply by the factor  $A_{\text{EFF}}$ . For nuclei much heavier than Be, the relation  $A_{\text{EFF}} = A^{0.9}$  is likely to be modified because of the opposing effects of (a) nuclear absorption of the photoproduced kaons and (b) production of kaons in multistep processes such as  $\gamma N \rightarrow \pi X$ ,  $\pi N \rightarrow KX'$ .



As a further test of the present analysis, we compare in Fig. 11 the average of  $K^+$  and  $K^-$  photoproduction yields from electrons on Be targets<sup>(46-48)</sup> to the expected  $K_L^0$  yields.<sup>(49)</sup> Generally reasonable agreement is found although there are large systematic differences between the experiments.

Extrapolations of  $K_L^0$  yields to higher energies for several different Be target thicknesses have also been made. The yields for  $2^\circ$  production from a 1.0 r.l. Be target at energies of 30, 40, and 50 GeV are given in Fig. 12. The yields for  $2^\circ$  production from 0.5, 1.0, and 2.0 radiation length Be targets at an energy of 40 GeV are given in Fig. 13.

In conclusion, the interpretation presented in this paper successfully describes the  $K_L^0$  photoproduction yields, together with the average of  $K^+$  and  $K^-$  photoproduction yields, over a wide range of electron energies, production angles, and target thicknesses. In addition, we find that the inclusive photoproduction of particles from light nuclei and from hydrogen appear to be related simply by a multiplicative factor,  $A_{EFF}$ , the effective number of nucleons in the target nucleus. The success of the inclusive interpretation allows us with confidence to extrapolate  $K_L^0$  yields to 50 GeV.

We wish to thank A. Kilert, W. Walsh, A. Baumgarten, and R. Vetterlein for help in design and construction of the neutral beam. We are grateful for the assistance given to us by R. Watt and the crew of the SLAC 40-inch bubble chamber, by J. Brown and the film analysis group at SLAC, and by D. Johnson.

## REFERENCES

1. A. D. Brody, W. B. Johnson, D. W. G. S. Leith, G. Loew, J. S. Loos, G. Luste, R. Miller, K. Moriyasu, B. C. Shen, W. M. Smart, and R. Yamartino, *Phys. Rev. Letters* 22, 966 (1969).
2. D. G. Cassel, E. Engels, Jr., A. C. Entis, and A. Sadoff, *Phys. Letters* 34B, 223 (1971).
3. M. G. Albrow, D. Aston, D. P. Barber, L. Bird, R. J. Ellison, C. Halliwell, A. E. Harckham, F. K. Loebinger, P. G. Murphy, J. Walters, A. J. Wynroe, and R. F. Templeman, *Nucl. Phys.* B23, 509 (1970).
4. J. F. Shivell, E. Engels, Jr., A. Entis, J. M. Paterson, L. N. Hand, and A. Sadoff, *Phys. Rev. Letters* 19, 1349 (1967).
5. C. D. Buchanan, C. Y. Chien, B. Cox, E. Dally, D. F. Drickey, L. Ettlinger, P. Innocenti, F. D. Rudnick, E. Seppi, P. F. Shepard, D. H. Stork, H. K. Ticho, R. A. Zdanis, D. Berk, A. Grigorian, and L. Resvanis, *Phys. Lett.* 32B, 396 (1970).
6. R. S. Larsen and D. Horelick, *A Precision Toroidal Charge Monitor for SLAC*, SLAC-PUB-398 (1968).
7. A small fraction of true  $K_{e3}$  decays failed to have a kinematic solution due to measurement resolution or small angle scatters on the electron track. Events in this category are readily identifiable and have been included in the analysis of the  $K_L^0$  spectrum. Only 7% of the total sample are in this category.
8. The lifetime and decay properties of  $K_L^0$  and  $\phi(1020)$  mesons are taken from the compilation of the Particle Data Group, *Phys. Lett.* 39B, 1 (1972).
9. The Monte Carlo calculations have been done using the values  $\xi(0) = -0.85$ ,  $\lambda_+ = 0.045$  (parameters for the leptonic decay), and  $A = -0.25$  (parameter for the  $\pi^+ \pi^- \pi^0$  decay). However, the  $K_L^0$  momentum spectrum determined in

the present analysis is insensitive to the choice of matrix element parameters. A sample analysis using simple phase space for the Monte Carlo events produced a  $K_L^0$  momentum spectrum well within the statistical uncertainties.

10. In order to insure a smooth behavior of the  $\alpha_j^*$  versus  $P_K$ , a contribution is added to  $\chi^2$  which for the  $j^{\text{th}}$  bin is proportional to

$$\left[ \left( \frac{\alpha_{j+1} - \alpha_j}{\Delta P_{Kj}} \right) - \left( \frac{\alpha_j - \alpha_{j-1}}{\Delta P_{Kj-1}} \right) \right]^2 .$$

This additional term forces a smooth behavior of  $\frac{dZ(P_K)}{dP_K}$  without significantly changing the original  $\chi^2$  value.

11. A. Böhm, P. Darriulat, C. Grosso, V. Kaftanov, K. Kleinknecht, H. L. Lynch, C. Rubbia, H. Ticho and K. Tittel, Nucl. Phys. B9, 605 (1969).
12. W. L. Lakin, E. B. Hughes, L. H. O'Neill, J. N. Otis, and L. Madansky, Phys. Letters 31B, 677 (1970).
13. R. J. Abrams, R. L. Cool, G. Giacomelli, T. F. Kycia, B. A. Leontic, K. K. Li, A. Lundby, D. N. Michael, and J. Teiger, Phys. Rev. D4, 3235 (1971).
14. The  $K_L^0$  - Pb absorption cross sections have been measured by comparing the  $K_L^0$  flux at the chamber with and without an additional  $130 \text{ g/cm}^2$  Pb in the neutral beam.
15. Expressing  $P_K$  in GeV/c and  $\sigma$  in mb, the parameters for the best fits to the cross section are:  $b_1 = 14.76$ ,  $b_2 = 0.00423$ ,  $b_3 = 19.21$ ,  $n_1 = 0.754$ ,  $n_2 = 0.874$ ,  $b_4 = 7.63$ ,  $b_5 = 17.50$ , and  $n_3 = 0.804$ .
16. R. L. Cool, G. Giacomelli, T. F. Kycia, B. A. Leontic, K. K. Li, A. Lunby, J. Tieger, and C. Wilkin, Phys. Rev. D1, 1887 (1970).
17. R. J. Abrams, R. L. Cool, G. Giacomelli, T. F. Kycia, B. A. Leontic, K. K. Li, and D. N. Michael, Phys. Rev. D1, 1917 (1970).
18. W. Galbraith, E. W. Jenkins, T. F. Kycia, B. A. Leontic, R. H. Phillips,

- A. L. Read, and R. Rubinstein, Phys. Rev. 138, B913 (1965).
19. A. P. Batson, B. B. Culwick, H. B. Klepp, and L. Riddiford, Proc. of the Royal Soc. (London) 251, 233 (1959).
  20. H. O. Cohn, R. D. McCulloch, W. M. Bugg, and G. T. Condo, Nucl. Phys. B21, 505 (1970).
  21. D. C. Brunt, M. J. Clayton, and B. A. Westwood, Phys. Rev. 187, 1856 (1969).
  22. A. Shapira, O. Benary, Y. Eisenberg, E. E. Ronat, D. Yaffe, and G. Yekutieli, Phys. Rev. Letters 21, 1835 (1968).
  23. J. G. Rushbrooke, D. V. Bugg, A. J. Oxley, J. A. Zoll, M. Jobes, J. Kinson, L. Riddiford, and B. Tallini, Nuovo Cimento 33, 1509 (1964).
  24. A. Gasparyan, A. V. Nikitin, and Yu. A. Troyan, Preprint-JINR-PI-5665, Dubna (1971).
  25. W. Schimmerling, T. J. Devlin, W. W. Johnson, K. G. Vosburgh, and R. E. Mischke, Rutgers Univ. Preprint (Feb., 1972).
  26. N. E. Booth, G. W. Hutchinson, and B. Ledley, Proc Phys. Soc. (London) 71, 293 (1958).
  27. T. Coor, D. A. Hill, W. F. Hornyak, L. W. Smith, and G. Snow, Phys. Rev. 98, 1369 (1955).
  28. V. P. Dzhelepov, V. I. Satarov, and B. M. Golovin, Soviet Phys. JETP 2, 293, (1959).
  29. E. F. Parker, T. Dobrowolski, H. R. Gustafson, L. W. Jones, M. J. Longo, F. E. Ringia, and B. Cork, Phys. Letters 31B, 250 (1970).
  30. J. Engler, K. Horn, F. Mönnig, P. Schludecker, W. Schmidt-Parzefall, H. Schopper, P. Sievers, H. Ullrich, R. Hartung, K. Runge, and Yu. Galaktionov, Phys. Letters 32B, 716 (1970).
  31. R. E. Mischke, T. J. Devlin, W. Johnson, J. Norem, K. Vosburgh, and W. Schimmerling, Phys. Rev. Letters 25, 1724 (1970).

32. E. F. Parker, T. Dobrowolski, H. R. Gustafson, L. W. Jones, M. J. Longo, F. E. Ringia, and B. Cork, *Phys. Letters* 31B, 246 (1970).
33. J. Engler, K. Horn, J. König, F. Mönnig, P. Schludecker, H. Schopper, P. Sievers, H. Ullrich, and K. Runge, *Phys. Letters* 28B, 64 (1968).
34. The analagous production of particles by virtual photons (electroproduction) also occurs. However, for the present application we can ignore the electroproduction of particles since the ratio of the contribution of virtual/real photons is approximately  $0.02/T$ , where  $T$  is the target thickness in units of radiation lengths. For a further discussion, see L. Hand and R. Wilson, SLAC Report 25, Part II (1963).
35. Y. S. Tsai and Van Whitis, *Phys. Rev.* 149, 1248 (1966).
36. G. McClellan, N. Mistry, P. Mostek, H. Ogren, A. Osborne, J. Swartz, R. Talman, and G. Diambrini-Palazzi, *Phys. Rev. Letters* 26, 1593 (1971).
37. R. P. Feynman, *Phys. Rev. Letters* 23, 1415 (1969).
38. For a review of inclusive reactions, see for example, W. R. Frazer, L. Ingber, C. H. Mehta, C. H. Poon, D. Silverman, K. Stowe, P. D. Ting, and H. J. Yesian, *Rev. Mod. Phys.* 44, 284 (1972).
39. N. F. Bali, L. S. Brown, R. D. Peccei, and A. Pignotti, *Phys. Rev. Letters* 25, 557 (1970).
40. J. L. Day, N. P. Johnson, A. D. Krisch, M. L. Marshak, J. K. Randolph, P. Schmueser, G. J. Marmer, and L. G. Ratner, *Phys. Rev. Letters* 23, 1055 (1969).
41. K. C. Moffeit, J. Ballam, G. B. Chadwick, M. Della-Negra, R. Gearhart, J. J. Murray, P. Seyboth, C. K. Sinclair, I. O. Skillicorn, H. Spitzer, G. Wolf, H. H. Bingham, W. B. Fretter, W. J. Podolsky, M. S. Rabin, A. H. Rosenfeld, R. Windmolders, G. P. Yost, and R. H. Milburn, *Phys. Rev.* D5, 1603 (1972).

42. A.M. Boyarski, D. Coward, S. Ecklund, B. Richter, D. Sherden, R. Siemann, and C. Sinclair, Inclusive Yields of  $\pi^+$ ,  $\pi^-$ ,  $K^+$ , and  $K^-$  from Hydrogen Photo-produced at 18 GeV at Forward Angles, paper submitted to the International Symposium of Electron and Photon Interactions at High Energies, Ithaca, N. Y. (1971); D. Sherden, private communication.
43. Values for  $\mathcal{F}(x)$  for hydrogen have been evaluated from the data in Ref. 41 by assuming  $E^* \frac{d^3\sigma}{d^3p} = B \exp(-Bp_{\perp}^2) \mathcal{F}(x)$ , and using  $B = 4.4 \text{ GeV}^{-2}$ . In making the comparison of  $K_L^0$  photoproduction from Be with  $K^{\pm}$  photoproduction from hydrogen, we ignore possible systematic differences due to isospin and regeneration.
44. D.O. Caldwell, V.B. Elings, W.P. Hesse, G.E. Jahn, R.J. Morrison, F.V. Murphy, and D.E. Yount, Phys. Rev. Letters 23, 1256 (1969).
45. V. Heynen, H. Meyer, B. Naroska, and D. Notz, Phys. Letters 34B, 651 (1971).
46. A. Barna, J. Cox, F. Martin, M.L. Perl, T. H. Tan, W.T. Toner, T.F. Zipf, and E.H. Bellamy, Phys. Rev. Letters 18, 360 (1967).
47. S.M. Flatté, J.J. Murray, P.R. Klein, L.H. Johnston, S.G. Wojcicki, Phys. Rev. 166, 1482 (1968).
48. A.M. Boyarski, F. Bulos, W. Busza, R. Diebold, S.D. Ecklund, G.E. Fischer, J.R. Rees, and B. Richter, SLAC Users Handbook, Section C.2 (Oct. 1971).
49. The calculated curves are identical to the expected  $K_L^0$  yields except that the branching ratio of  $\phi(1020)$  into charged kaons has been used (see Ref. 8).

## FIGURE CAPTIONS

1. Schematic illustration of the neutral secondary beam.
2. Distribution in  $p_{\text{VIS}}$  used to determine the  $K_L^0$  momentum spectrum from 16 GeV electrons incident at  $2^\circ$  production angle on a 1.75 r.l. Be target. The variable  $p_{\text{VIS}}$  is the visible momentum from the three body  $K_L^0$  decays, as explained in the text. (a) - (s) Monte Carlo generated component histograms corresponding to the indicated narrow  $K_L^0$  momentum intervals. The intensities of the histograms are determined by a fit to the  $p_{\text{VIS}}$  spectrum. (t) Experimental  $p_{\text{VIS}}$  spectrum. The solid curve is the summation of the fitted component histograms.
3. Comparison of the  $K_L^0$  flux (circles) and neutron flux (squares) at the hydrogen bubble chamber. This comparison is a typical example of the relative  $K_L^0/n$  fluxes at the experimental apparatus, but this ratio does depend on the amount of photon absorber in the beam, the production angle, and the distance between the target and apparatus. The solid and open circles result from different methods of analysis of the  $K_L^0$  spectrum (see text).
4. Absorption cross sections for K mesons on various absorbers. The data are from the following sources: ( $\blacksquare$ )  $K_L^0$  - Pb (this experiment); ( $\blacktriangle$ )  $K_L^0$  - Pb,  $K_L^0$  - Cu, and  $K_L^0$  - C ( Ref. 12); ( $\bullet$ ) average of  $K^+$  and  $K^-$  on Cu, C, and n (Ref. 13, 16, 17); ( $\diamond$ ) average of  $K^+$  and  $K^-$  on n (Ref. 18). The curves shown are empirical interpolations described in the text.
5. Yields of  $K_L^0$  mesons from electrons incident on a 1.75 r.l. Be target. The various electron energies and production angles are indicated. The curves represent an interpretation of the yields (discussed in detail in the text) in terms of the inclusive  $K_L^0$  photoproduction from the individual nucleons in the Be nucleus together with the coherent  $\phi(1020)$  photoproduction from the entire nucleus. The sum of these two processes is shown by the solid curves, whereas the inclusive

production alone is shown by the dashed curves.

6. Yields of  $K_L^0$  mesons from electrons incident on an 0.70 r.l. Be target. The electron energies and production angles are indicated. The meaning of the curves is discussed in the caption to Figure 5.
7. Summary of cross section values for the reaction  $np \rightarrow pp\pi^-$ . The inset shows the low energy data on an expanded momentum scale. The data sources are: ( $\triangle$ ) Ref. 19, ( $\nabla$ ) Ref. 20, ( $\square$ ) Ref. 21, ( $\times$ ) Ref. 22, ( $\bullet$ ) Ref. 23, and ( $\circ$ ) Ref. 24. The solid curve is a hand drawn interpolation curve used to extract neutron flux at the chamber. The dashed curves represent our estimate of the uncertainty in the extrapolation curve.
8. Yields of neutrons from electrons incident on a 1.75 r.l. Be target. The electron energies and production angles are indicated.
9. Calculated yields for successive bins in  $\mathcal{F}(x)$ . The different curves result from distinct bins in  $\mathcal{F}(x)$  which have widths of 0.1 in  $x$  and are centered at the indicated values of  $x$  (see text).
10. Integrated structure function,  $\mathcal{F}(x)$ , versus  $x$ . The solid circles are the values found in the present analysis for  $K_L^0$  photoproduction from Be. For comparison, the average of  $K^+$  and  $K^-$  data from hydrogen (Ref. 42) are also shown. The hydrogen data are multiplied by a factor,  $A_{\text{EFF}} = 6$ , in order to account for the Be target (see text).
11. Comparison of expected yields for  $K_L^0$  from Be to the average of  $K^+$  and  $K^-$  yields from Be. The data sources are: ( $\blacklozenge$ ) Ref. 46, ( $\blacklozenge$ ) Ref. 47, and ( $\blacklozenge$ ) Ref. 48. The electron energies, production angles, and target thicknesses are indicated. The curves are calculated from the fitted values for  $\mathcal{F}(x)$  as explained in the text. The solid and dashed curves are as in the caption to Figure 5.
12. Predicted yields of  $K_L^0$  mesons for  $2^\circ$  production from a 1.0 r.l. Be target



at electron energies of 30, 40, and 50 GeV.

13. Predicted yields of  $K_L^0$  mesons for  $2^0$  production from 0.5, 1.0, and 2.0 r.l.

Be targets at an electron energy of 40 GeV.

Table 1

Target thicknesses, electron energies, and production angles for  
 $K_L^0$  and n yields in the present experiment

Experimental Run	Thickness of Be Target (r.l.)	e <sup>-</sup> Energy (GeV)	Production Angle (degrees)	Particle Yields Reported
I	1.75	10	2	$K_L^0$
			4	$K_L^0$
		16	2	$K_L^0$ and n
			3	$K_L^0$ and n
			4	$K_L^0$ and n
II	0.70	16	1.6	$K_L^0$
		18	1.6	$K_L^0$
III	1.75	19	1.6	$K_L^0$ and n

Table 2

Photon absorbers used in secondary neutral beams

e <sup>-</sup> Energy (GeV)	Production Angle	Amount of material in secondary beam (g/cm <sup>2</sup> )			
		Hydrogen <sup>a</sup>	Lithium <sup>a</sup>	Tungsten	Lead
10	2°	6.5	44.6	147.1	173.0
10	4°	6.5	44.6	147.1	173.0
16	2°	6.5	44.6	147.1	173.0
16	3°	6.5	44.6	147.1	173.0
16	4°	6.5	44.6	147.1	173.0
16	1.6°	9.7	65.0	98.0	216.2
18	1.6°	9.7	65.0	98.0	259.5
19	1.6°	3.3	22.3	98.0	230.6

a. The hydrogen and lithium was in the form of compressed blocks of lithium hydride powder kept in an inert atmosphere.

Table 3  $K_L^0$ -Pb Absorption Cross Sections

$K_L^0$ Momentum (GeV/c)	$\sigma^a$ (mb)
1.4 - 2.6	$2730 \pm 100$
2.6 - 3.4	$2660 \pm 120$
3.4 - 5.0	$2540 \pm 130$
5.0 - 7.4	$2370 \pm 140$

- a. The uncertainties quoted are statistical only. The overall systematic error is estimated to be  $\pm 5\%$ .

Table 4

$K_L^0$  yields for electrons incident on 1.75 rad. length Be target

Electron Energy (GeV)	10	10	16	16	16	16	19
Production Angle	2°	4°	2°	3°	4°		1.6°
No. Events in $P_{VIS}$ Distribution	821	601	7112	2149	1524		2468
$K_L^0$ Momentum Interval (GeV/c)	Yield at target $K_L^0/(10^4 \text{ electrons})/\text{sr}/\text{GeV}/c$						
1.0 - 1.5	1.10 ± 0.13	1.12 ± 0.13	2.40 ± 0.12	1.92 ± 0.15	1.70 ± 0.20	2.40 ± 0.20	2.40 ± 0.20
1.5 - 2.0	1.18 ± 0.10	1.19 ± 0.11	2.59 ± 0.12	2.10 ± 0.13	1.89 ± 0.17	2.76 ± 0.15	2.76 ± 0.15
2.0 - 2.5	1.21 ± 0.10	1.12 ± 0.10	2.70 ± 0.12	2.15 ± 0.13	2.00 ± 0.16	3.00 ± 0.15	3.00 ± 0.15
2.5 - 3.0	1.19 ± 0.10	0.93 ± 0.09	2.62 ± 0.11	2.06 ± 0.12	1.99 ± 0.14	3.17 ± 0.15	3.17 ± 0.15
3.0 - 3.5	1.08 ± 0.11	0.65 ± 0.09	2.44 ± 0.11	1.89 ± 0.12	1.78 ± 0.12	3.13 ± 0.15	3.13 ± 0.15
3.5 - 4.0	0.86 ± 0.13	0.42 ± 0.08	2.14 ± 0.10	1.67 ± 0.11	1.53 ± 0.10	2.94 ± 0.15	2.94 ± 0.15
4.0 - 4.5	0.61 ± 0.11	0.27 ± 0.07	1.85 ± 0.10	1.46 ± 0.10	1.24 ± 0.09	2.70 ± 0.14	2.70 ± 0.14
4.5 - 5.0	0.38 ± 0.10	0.18 ± 0.06	1.58 ± 0.10	1.25 ± 0.09	1.01 ± 0.08	2.45 ± 0.14	2.45 ± 0.14
5.0 - 6.0	0.16 ± 0.06	0.12 ± 0.05	1.21 ± 0.09	0.96 ± 0.08	0.74 ± 0.07	2.10 ± 0.12	2.10 ± 0.12
6.0 - 7.0	0.06 ± 0.03		0.84 ± 0.07	0.62 ± 0.07	0.48 ± 0.06	1.66 ± 0.11	1.66 ± 0.11
7.0 - 8.0			0.54 ± 0.05	0.38 ± 0.05	0.32 ± 0.05	1.34 ± 0.10	1.34 ± 0.10
8.0 - 9.0			0.35 ± 0.04	0.23 ± 0.04	0.19 ± 0.05	1.04 ± 0.09	1.04 ± 0.09
9.0 - 10.0			0.21 ± 0.03	0.14 ± 0.04	0.01 ± 0.04	0.76 ± 0.08	0.76 ± 0.08
10.0 - 11.0			0.09 ± 0.03	0.07 ± 0.03		0.50 ± 0.07	0.50 ± 0.07
11.0 - 12.0			0.05 ± 0.02			0.31 ± 0.06	0.31 ± 0.06
12.0 - 13.0						0.17 ± 0.06	0.17 ± 0.06

Table 5

$K_L^0$  yields for electrons incident on 0.70 rad. length Be target

Electron Energy (GeV)	16	18
Production Angle	1.6°	1.6°
No. Events in P <sub>VIS</sub> Distribution	4195	2117
$K_L^0$ momentum interval (GeV/c)	Yield at target $K_L^0 / (10^4 \text{ electrons}) / \text{sr} / \text{GeV}/c$	
1.0 - 1.5	0.83 ± 0.09	0.92 ± 0.09
1.5 - 2.0	1.00 ± 0.08	1.09 ± 0.09
2.0 - 2.5	1.13 ± 0.08	1.21 ± 0.09
2.5 - 3.0	1.17 ± 0.07	1.27 ± 0.08
3.0 - 3.5	1.14 ± 0.07	1.24 ± 0.08
3.5 - 4.0	1.10 ± 0.07	1.20 ± 0.08
4.0 - 4.5	1.03 ± 0.07	1.11 ± 0.07
4.5 - 5.0	0.96 ± 0.07	1.04 ± 0.07
5.0 - 6.0	0.82 ± 0.07	0.89 ± 0.07
6.0 - 7.0	0.60 ± 0.06	0.68 ± 0.06
7.0 - 8.0	0.40 ± 0.05	0.50 ± 0.06
8.0 - 9.0	0.25 ± 0.04	0.36 ± 0.05
9.0 - 10.0	0.13 ± 0.03	0.26 ± 0.04
10.0 - 11.0	0.06 ± 0.02	0.16 ± 0.04
11.0 - 12.0		0.09 ± 0.03

Table 6

Neutron yields for electrons incident on 1.75 rad. length Be target

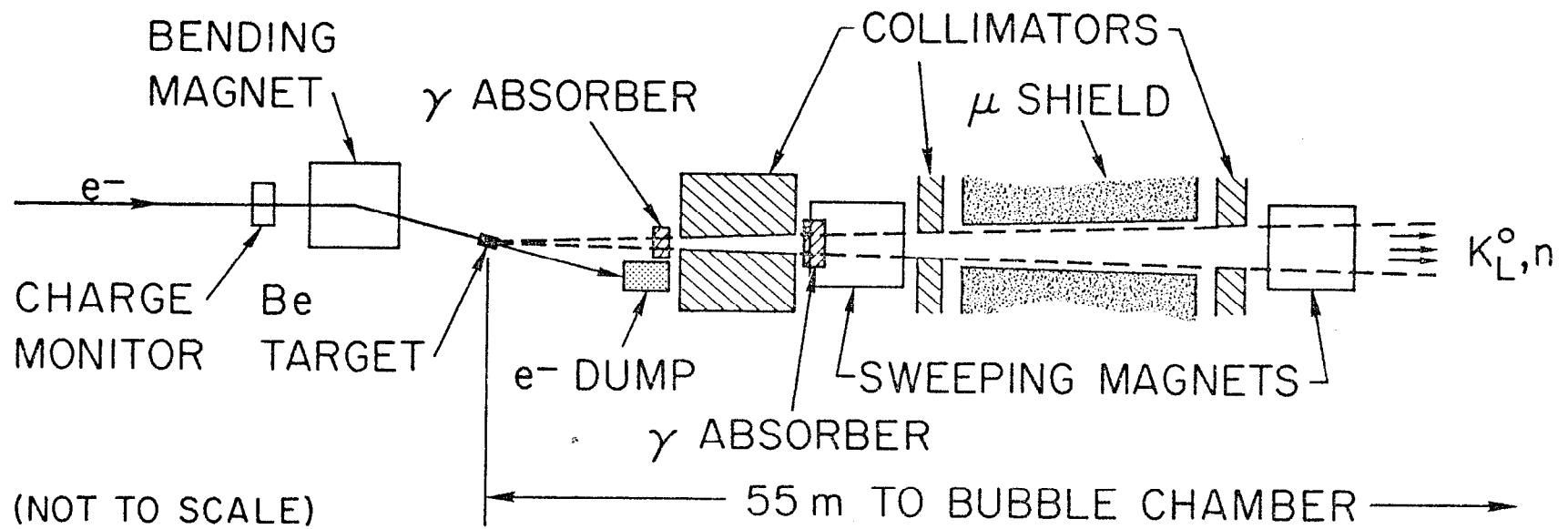
Electron Energy (GeV)	16	16	16	19
Production Angle	2°	3°	4°	1.6°
No. Events np → ppπ <sup>-</sup>	10596	3809	2722	3297
n Momentum Interval (GeV/c)	Yield at target n/(10 <sup>4</sup> electrons)/sr/GeV/c			
1.1 - 1.2	12.27 ± 3.00	11.22 ± 2.87	10.85 ± 2.81	10.34 ± 2.71
1.2 - 1.4	9.99 ± 1.31	9.52 ± 1.30	9.04 ± 1.26	9.13 ± 1.28
1.4 - 1.6	9.74 ± 1.10	8.15 ± 0.98	8.54 ± 1.04	8.41 ± 1.03
1.6 - 1.8	9.03 ± 1.04	8.99 ± 1.09	7.35 ± 0.93	8.83 ± 1.10
1.8 - 2.0	8.68 ± 0.86	7.35 ± 0.81	6.98 ± 0.80	7.60 ± 0.86
2.0 - 2.5	7.31 ± 0.75	6.52 ± 0.70	5.46 ± 0.61	6.84 ± 0.75
2.5 - 3.0	5.77 ± 0.66	5.47 ± 0.66	5.24 ± 0.65	5.40 ± 0.67
3.0 - 3.5	5.20 ± 0.67	4.33 ± 0.60	4.04 ± 0.58	5.00 ± 0.70
3.5 - 4.0	3.88 ± 0.56	3.91 ± 0.59	3.12 ± 0.50	3.87 ± 0.60
4.0 - 4.5	3.14 ± 0.50	3.45 ± 0.58	2.30 ± 0.42	4.09 ± 0.69
4.5 - 5.0	2.49 ± 0.44	2.20 ± 0.42	2.00 ± 0.40	3.30 ± 0.62
5.0 - 6.0	1.80 ± 0.28	1.56 ± 0.27	1.35 ± 0.24	2.57 ± 0.42
6.0 - 7.0	1.34 ± 0.24	1.24 ± 0.24	0.86 ± 0.19	1.78 ± 0.34
7.0 - 9.0	0.52 ± 0.10	0.53 ± 0.12	0.32 ± 0.08	1.03 ± 0.21

TABLE 7

Integrated Structure Function for  $\gamma\text{Be} \rightarrow \text{K}_L^0 \text{X}$ 

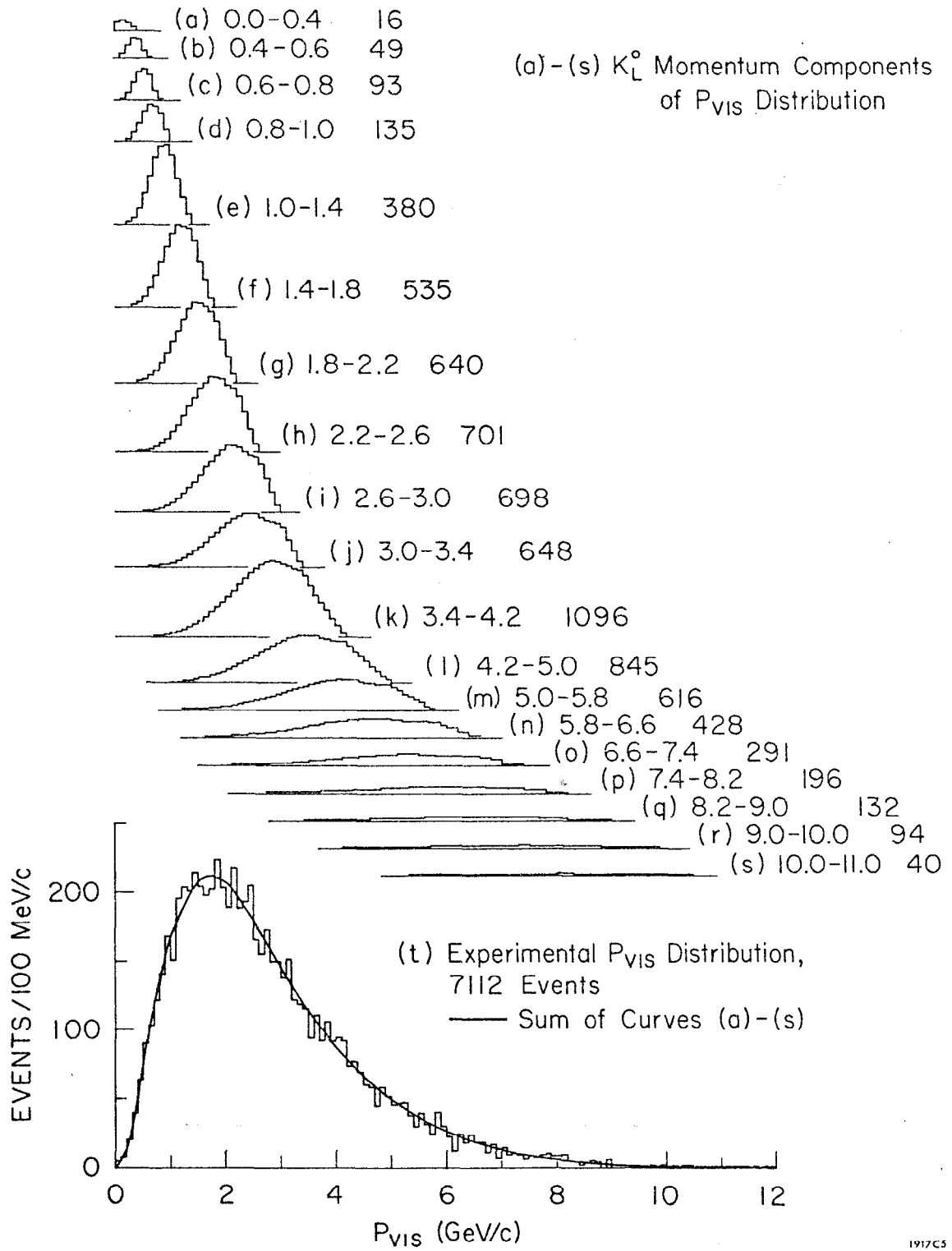
$x$	$\mathcal{F}(x)$ ( $\mu\text{b}$ )
0.0 - 0.2	$11.4 \pm 0.8$
0.2 - 0.3	$9.5 \pm 1.6$
0.3 - 0.4	$8.6 \pm 1.6$
0.4 - 0.5	$6.0 \pm 1.4$
0.5 - 0.6	$6.7 \pm 1.1$
0.6 - 0.7	$4.2 \pm 0.9$
0.7 - 0.9	$1.0 \pm 0.3$





191783

FIG. 1



1917C5

FIG. 2

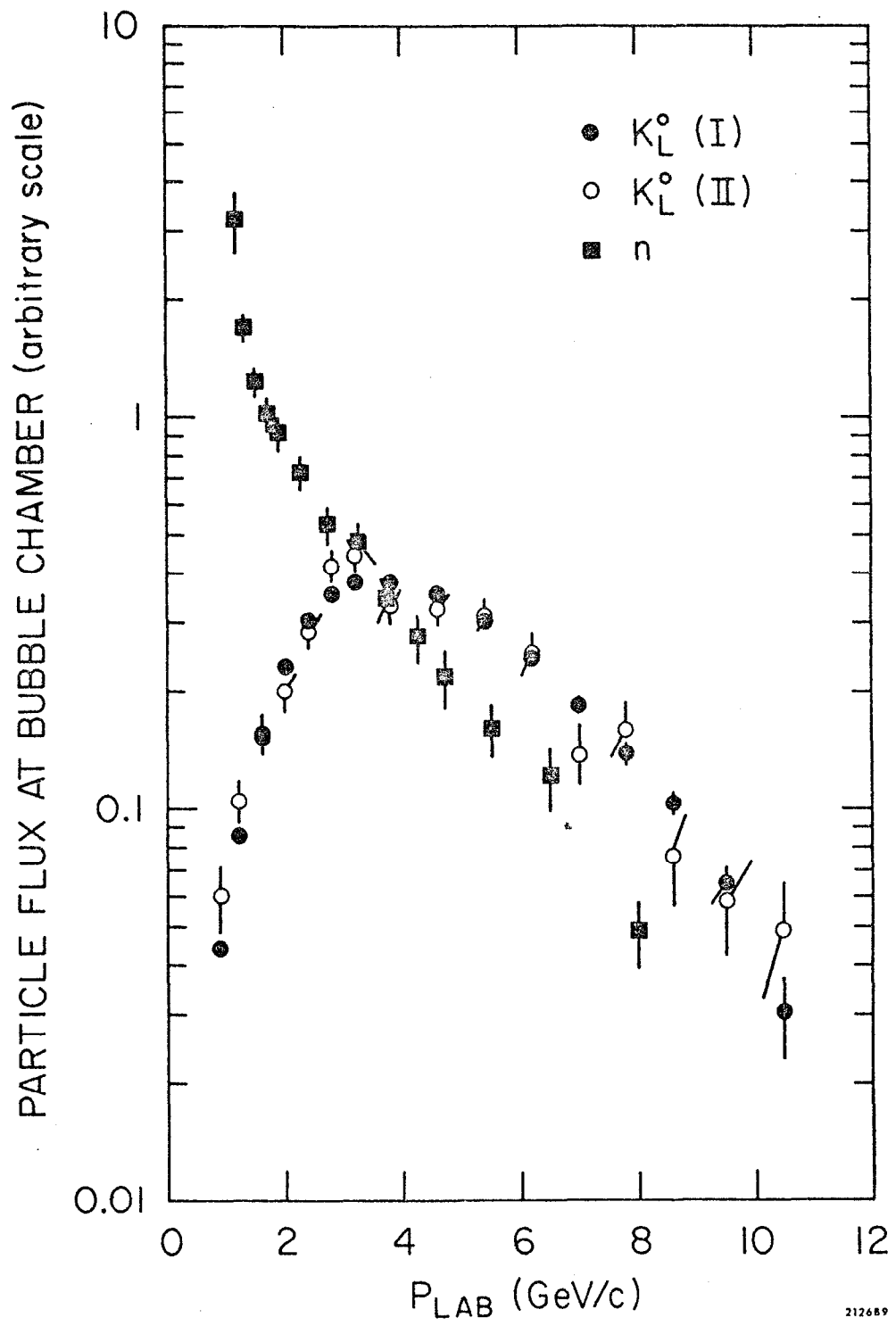


FIG. 3

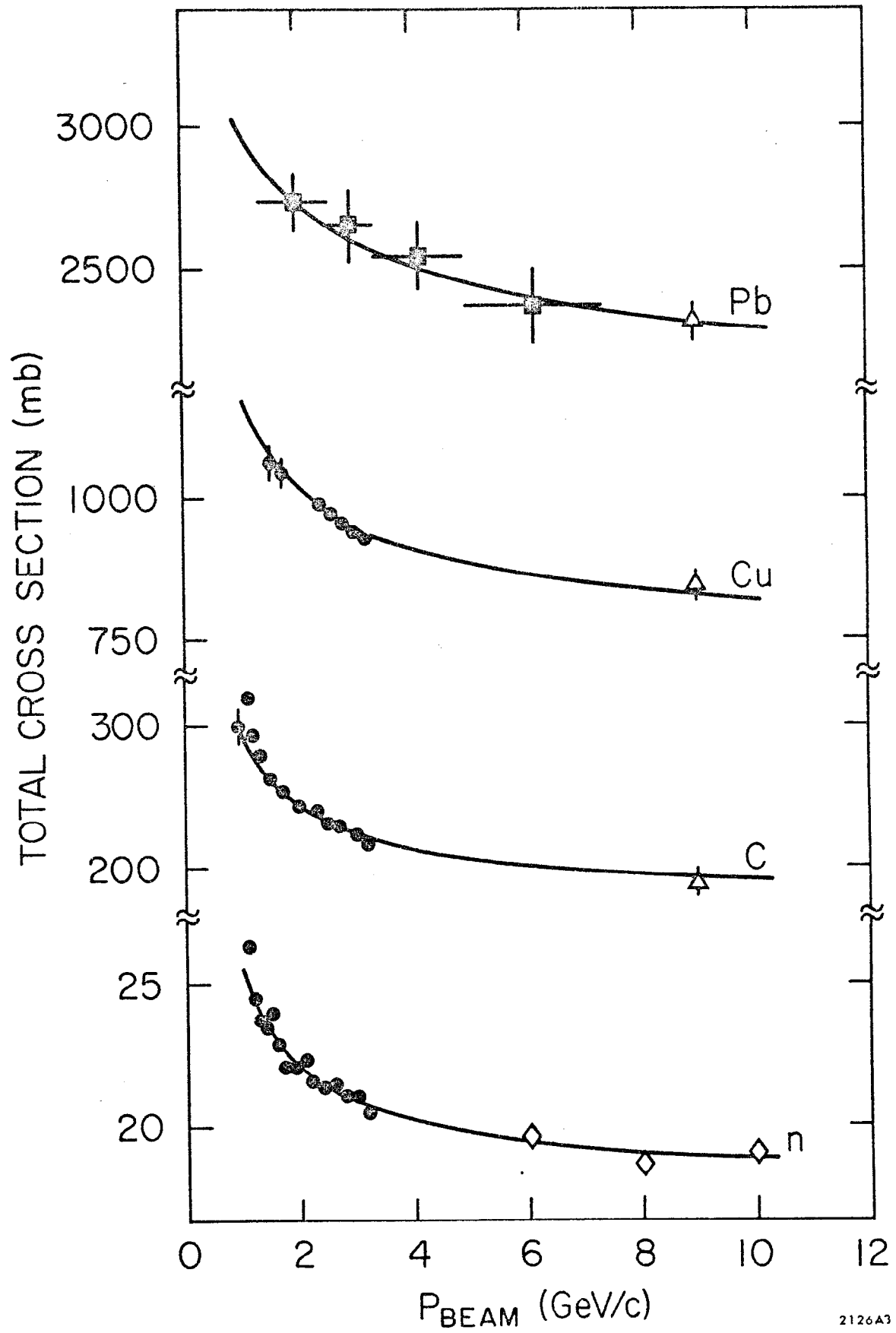


FIG. 4

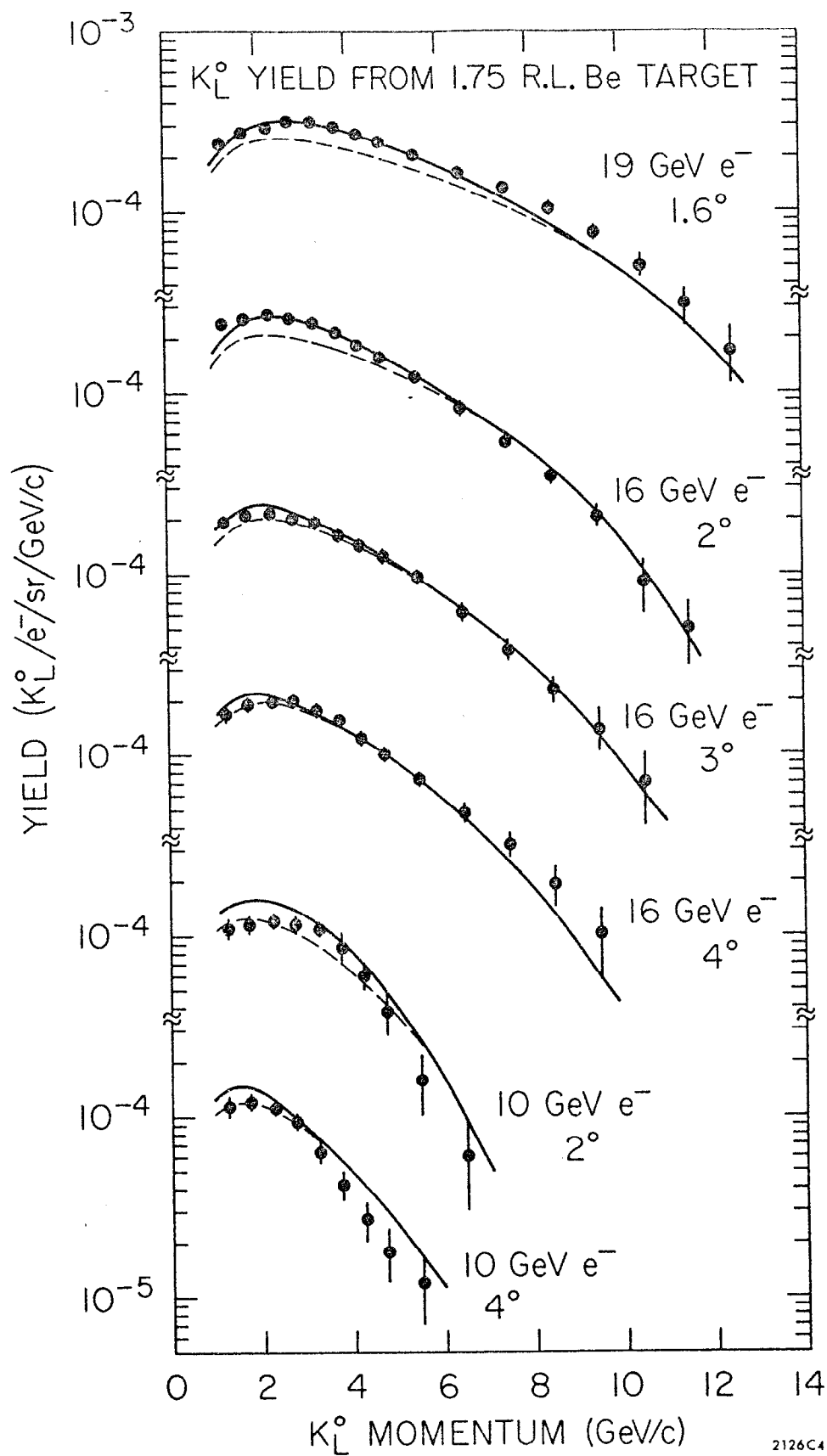
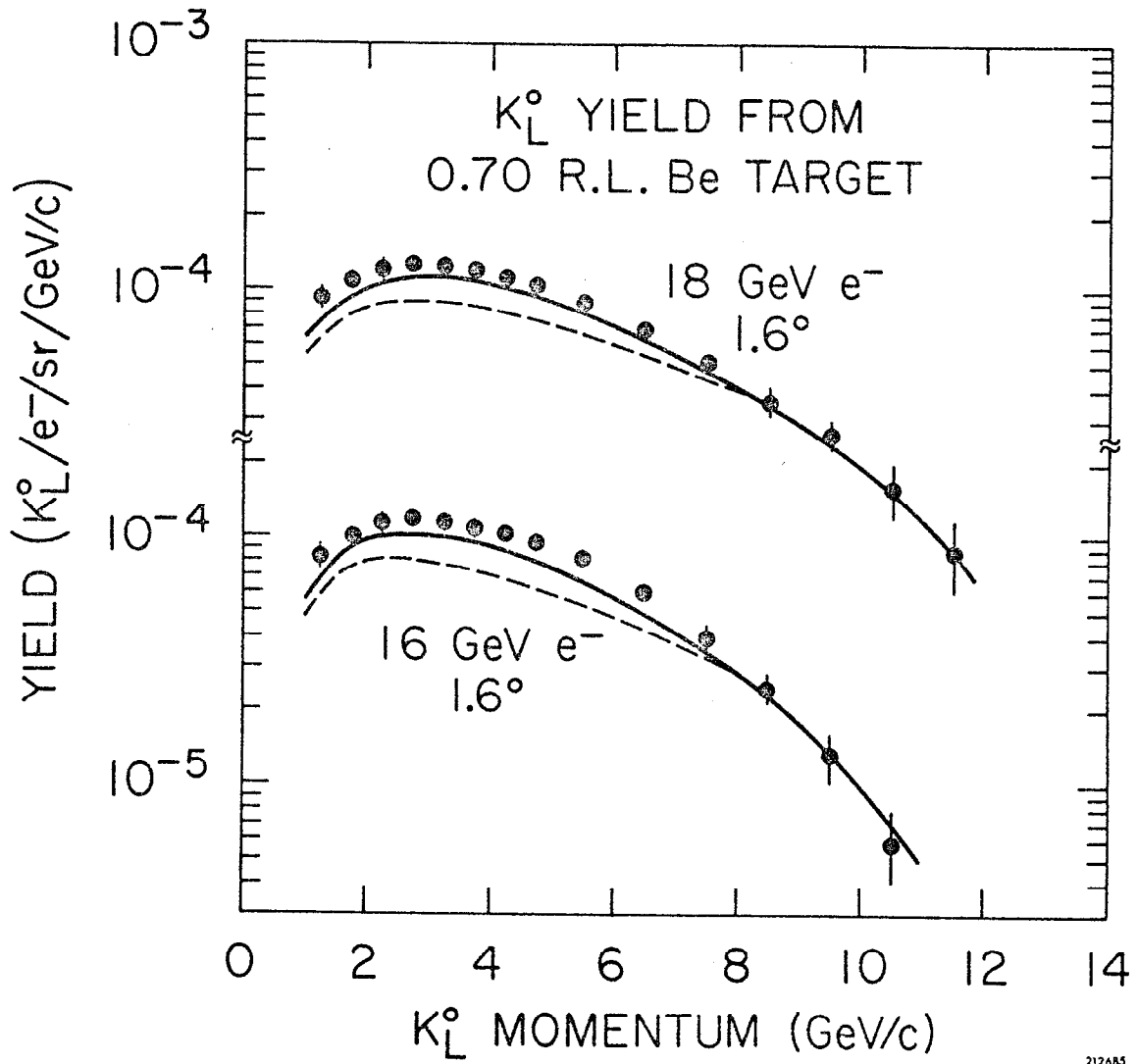


FIG. 5



212685

FIG. 6

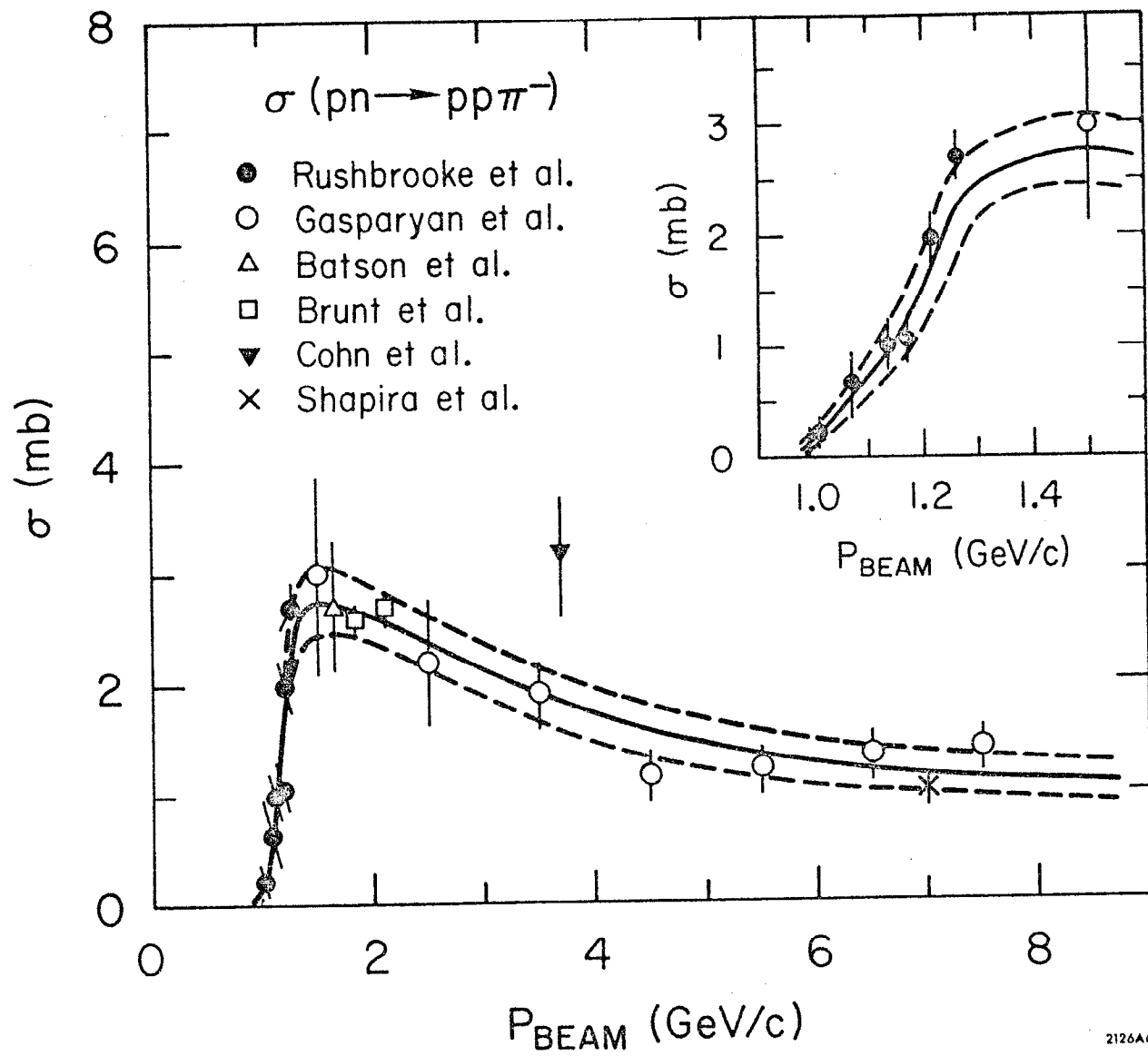
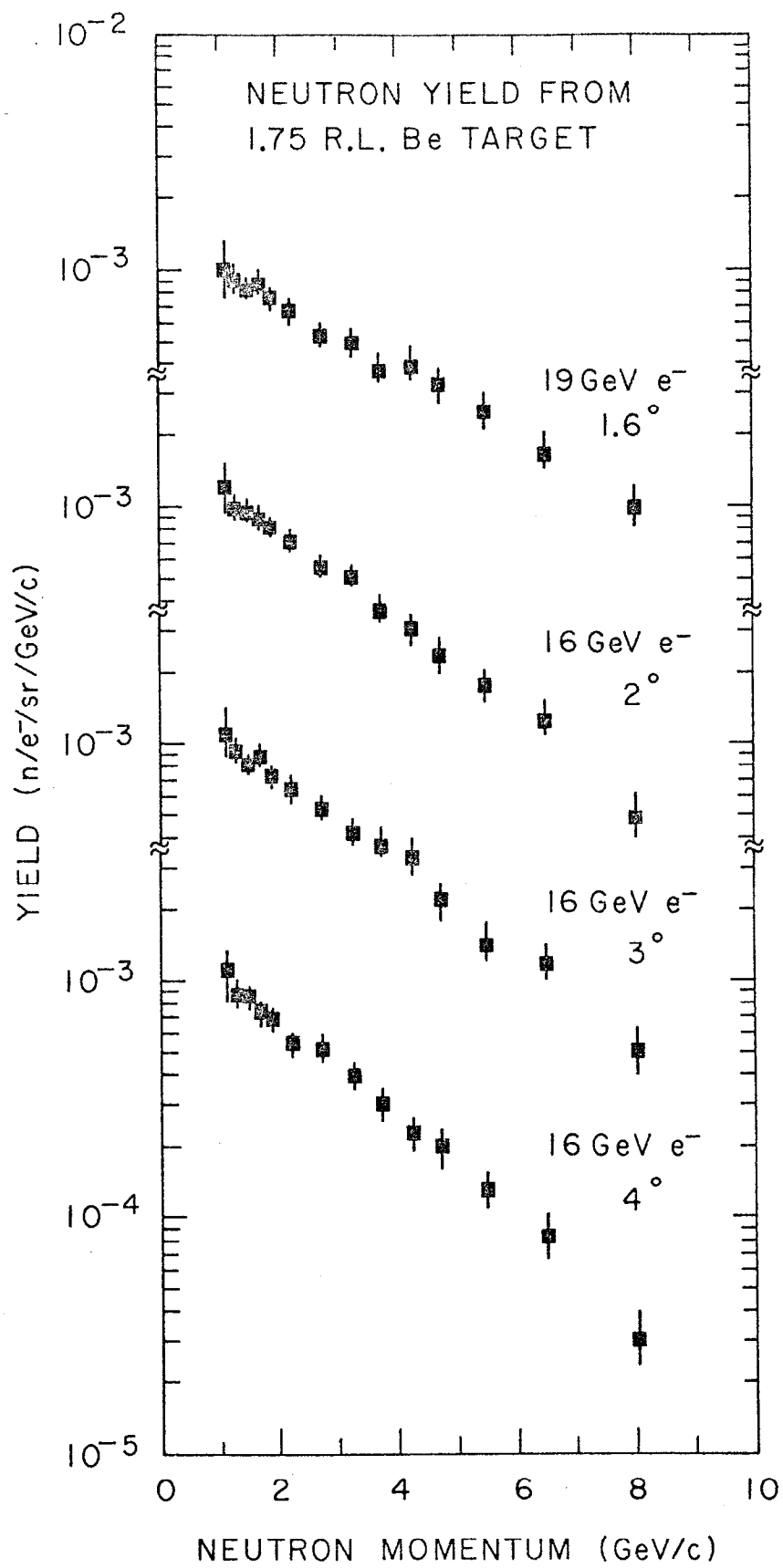


FIG. 7



212687

FIG. 8



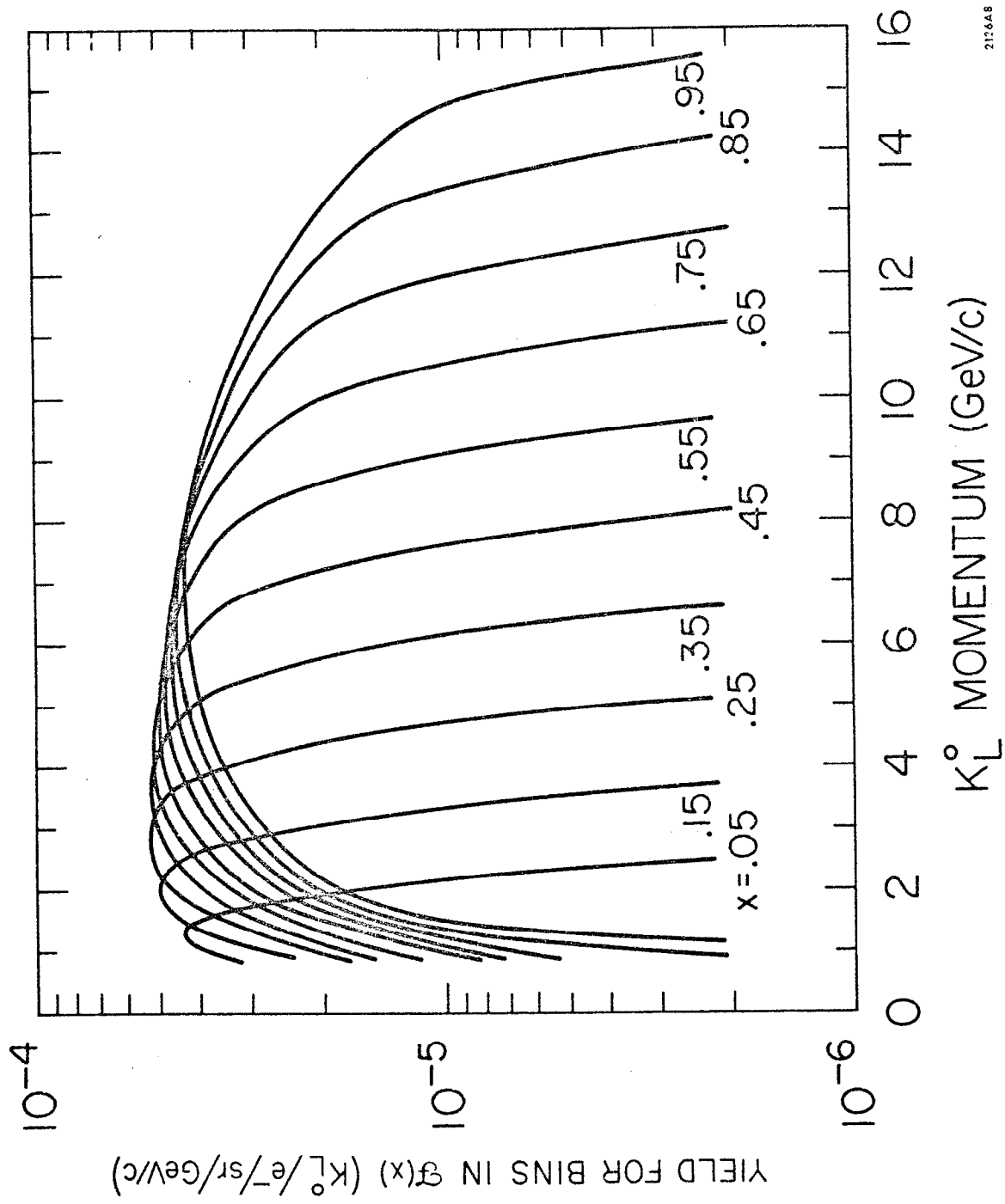


FIG. 9

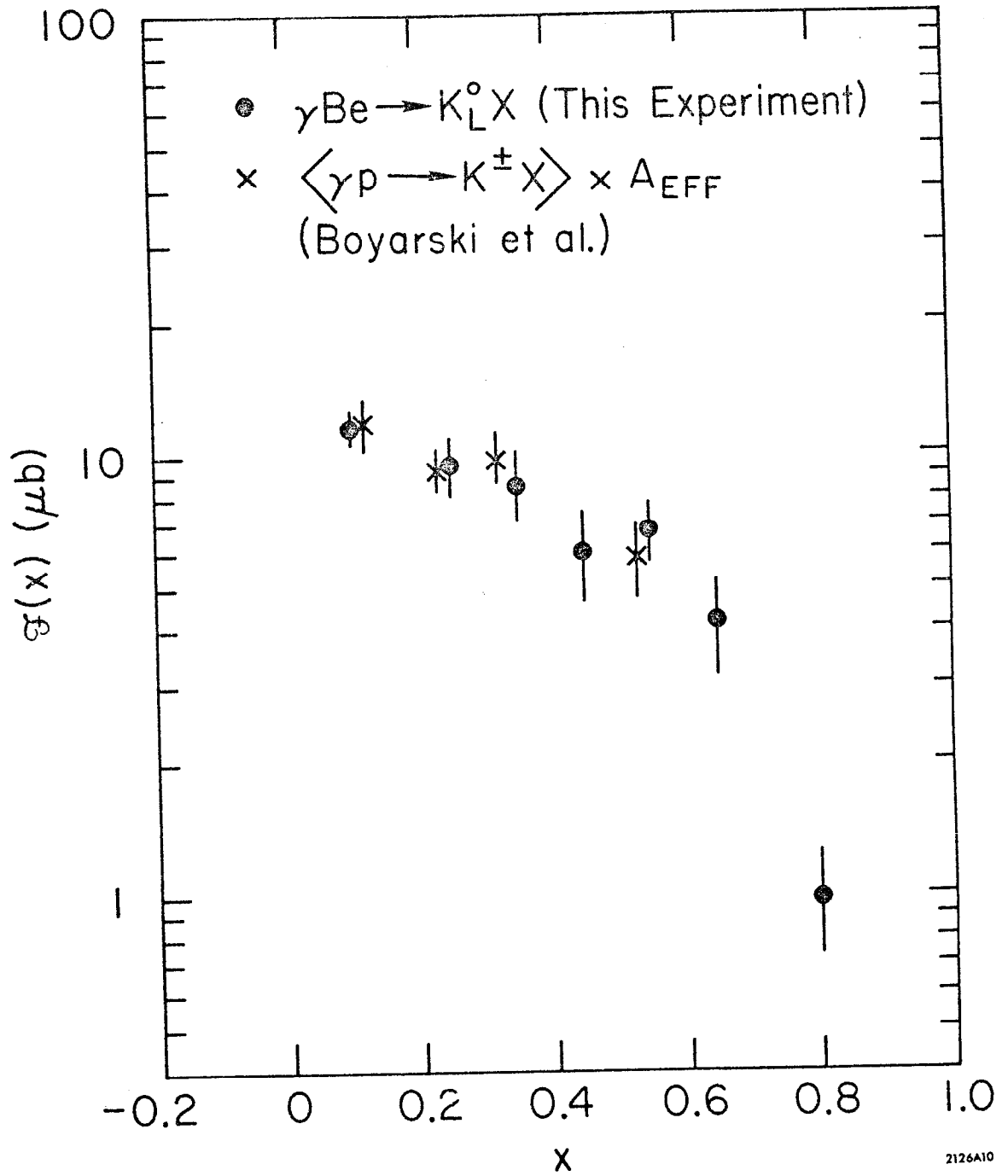


FIG. 10

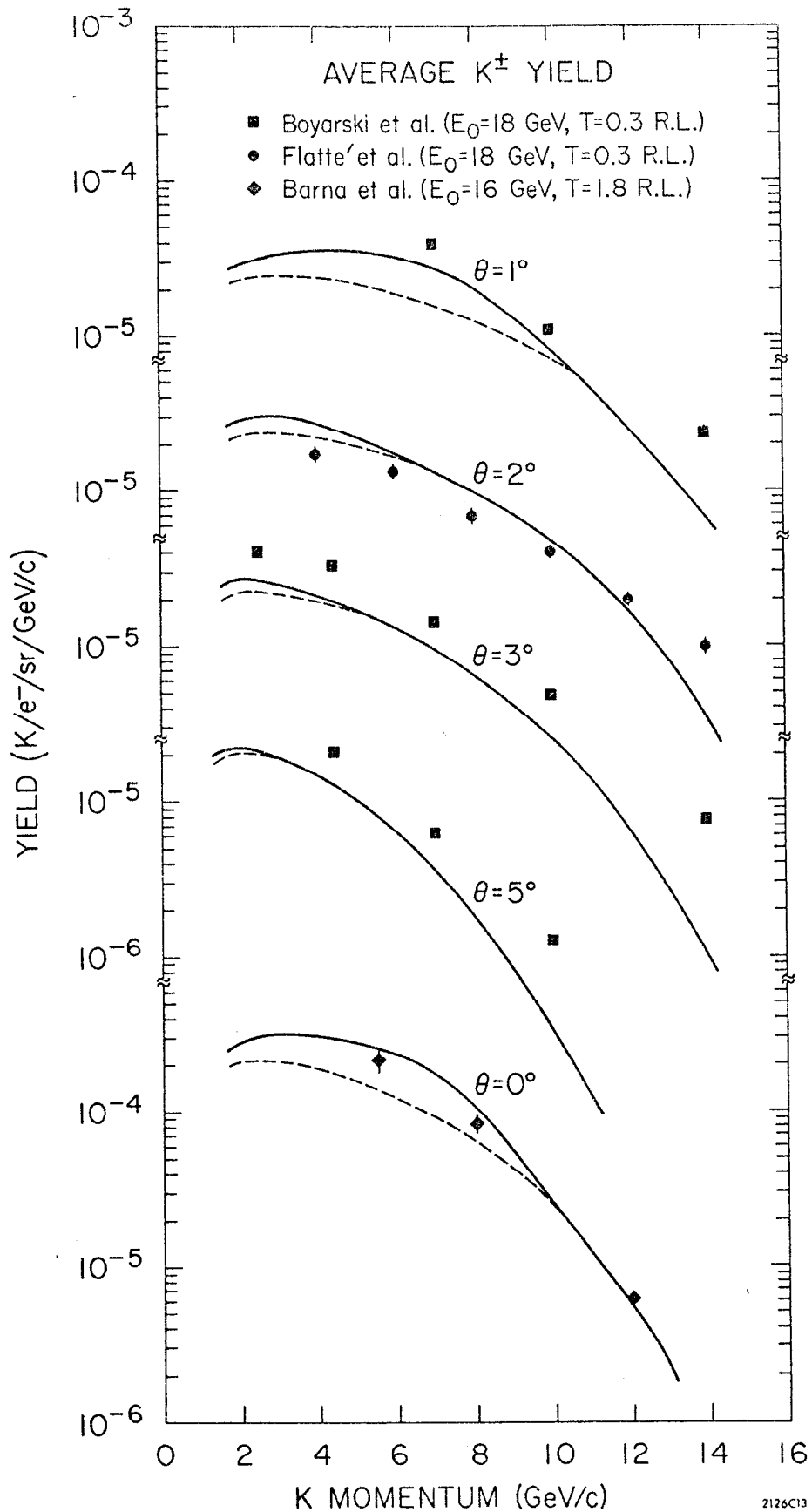


FIG. 11

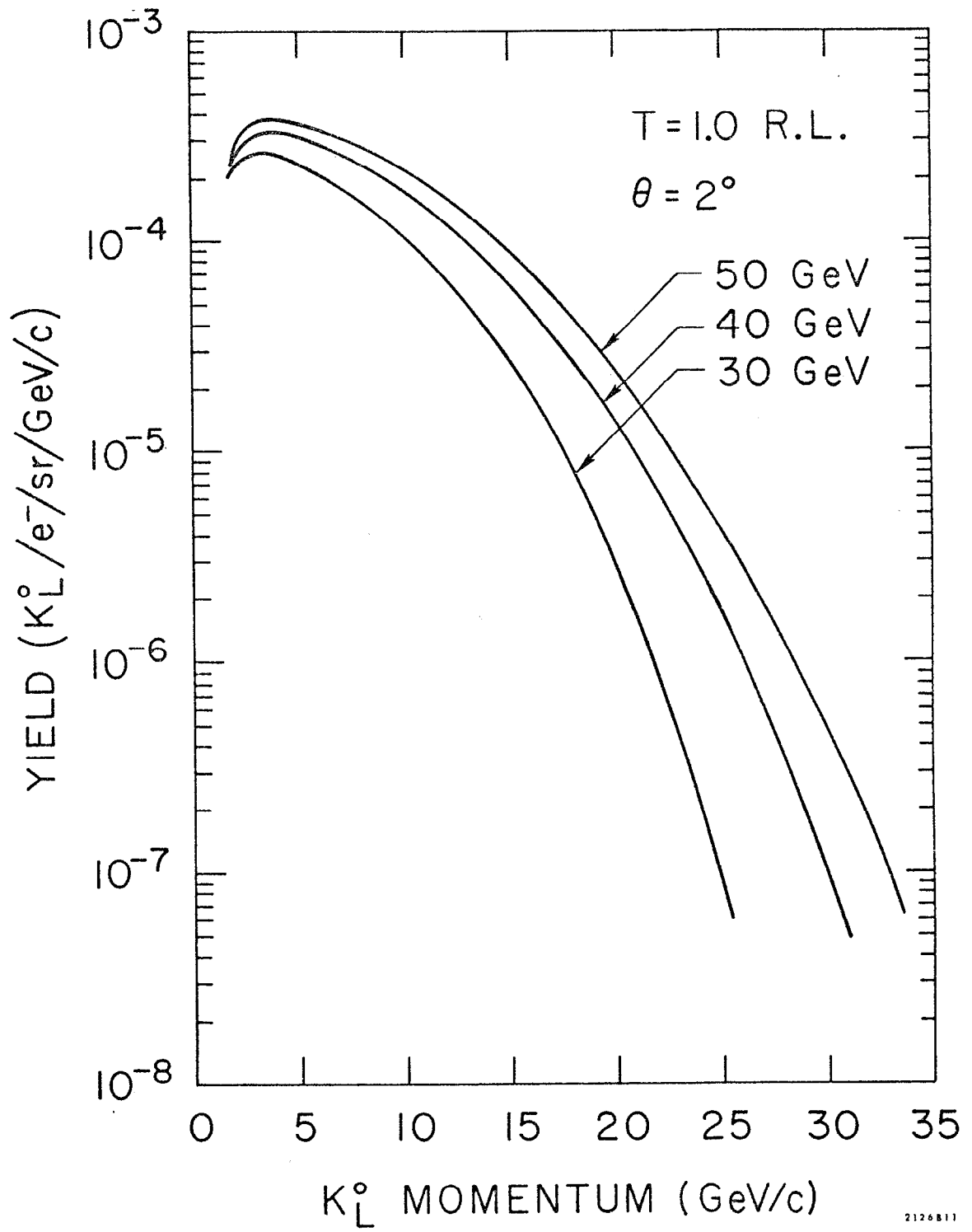


FIG. 12

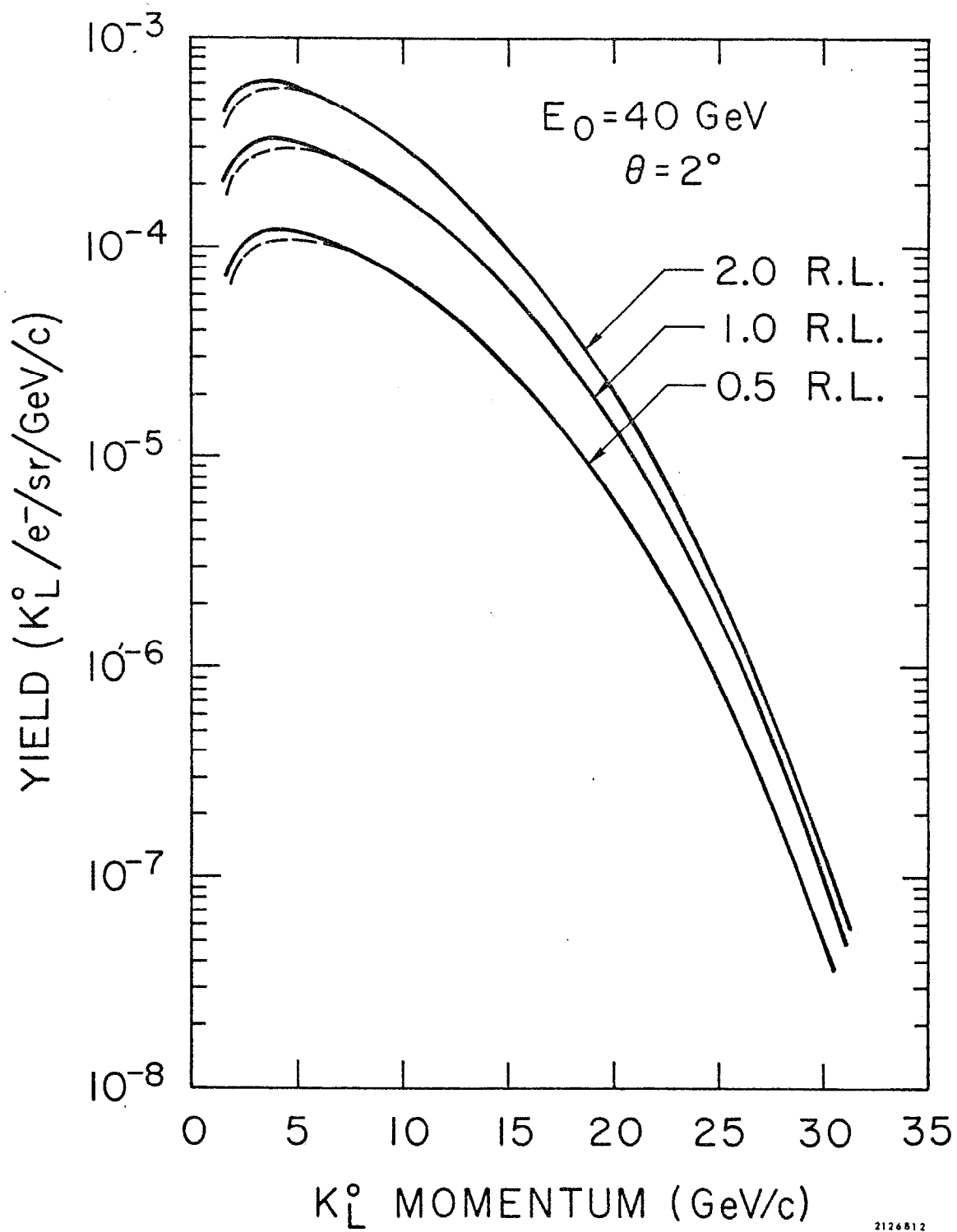


FIG. 13